PIV MEASUREMENTS IN A SEPARATING TURBULENT APG BOUNDARY LAYER

Kristian Angele
Department of Mechanics, KTH
S-100 44 Stockholm, Sweden
kristian@mech.kth.se

Barbro Muhammad-Klingmann
Department of Mechanics, KTH
S-100 44 Stockholm, Sweden
barbro@mech.kth.se

ABSTRACT

PIV and LDV were used to investigate a separating adverse pressure gradient (APG) turbulent boundary layer forming a long shallow separation bubble in near-equilibrium. The shape factor was approximately constant H_{12}=4 throughout the separation bubble.

The mean velocity profiles were found to be self-similar in Perry-Schofield coordinates and the Reynolds stresses were found to scale with the displacement thickness, δ^*, and their maximum value. This was located at y/δ^*=1, corresponding to approximately y^+=400. This coincidence between the inner and outer scale was found *at all x − positions*, indicating that there is only one length scale governing the flow.

EXPERIMENTAL SET-UP

The experiments were carried out at KTH in a wind-tunnel with a 4 meter long test section with cross section area 0.75 m x 0.5 m. The free stream velocity at the inlet of the test section in the experiments was 26.5 m/s. The temperature in the test section was kept constant at 20°C. For detailed information about the wind-tunnel see Lindgren (1999).

Flat plate

The boundary layer developed along a flat plate consisting of four 1 m long 20 mm thick plexiglass segments. The first segment has a super elliptic leading edge that is 200 mm long and symmetric. In order to fix the stagnation point on the leading edge the last 500 mm of the last segment was used as a flap.

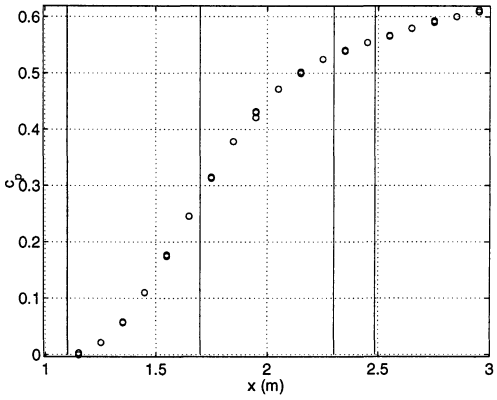

Figure 1: Wall static pressure distribution. Straight lines showing the position of the LDV measurements

Diffuser flow

The first 1.25 meter of the test section has a constant cross section area. After this the test section is diverged by using a flexible wall in order to achieve a diffuser-like flow.

Suction.

Suction is applied through small holes in the flexible wall in order to prevent the boundary layer from separating on the curved surface and induce an APG on the flat plate. 1300 holes with a diameter of 5 mm were connected to four suction boxes along 1 m of the diverging part between x=1250 and x=2250. These boxes are then connected via tubing to a 4.5 kW fan.

The flow removal due to the suction was estimated to be 6-7% of the total flow rate above the flat plate. This was verified by measuring the center line velocity with a Prandtl tube and LDV and assuming a parabolic profile at the exhaust of the fan. This corresponds to removing approximately the whole boundary

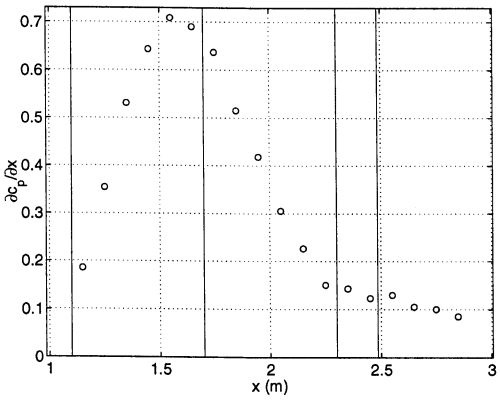

Figure 2: Pressure gradient. Straight lines showing the position of the LDV measurements

layer from the curved wall.

Trip

To trig a spanwise homogeneous transition the boundary layer was tripped using a 0.4 mm zig zag tape from Glasfaser Flugzeugbau Hansjörg Strejfender. The trip is placed 25 cm down stream of the tip of leading the edge i.e. 5 cm after the elliptical part of the leading edge. This arrangement assured a fully developed turbulent boundary layer well upstream of the expanding part of the test section.

Pressure taps

The flat plate is equipped with 48 pressure taps evenly distributed along the plate at every 100 mm after the first meter. Pressure taps are also placed in the spanwise direction 175 mm off the centerline at every second tap position after the first meter to check the homogeneity of the flow.

PRESSURE DISTRIBUTION

$$c_p = \frac{p - p_{ref}}{p_0 - p_{ref}} \qquad (1)$$

In Figure 1 the pressure coefficient c_p is plotted against the distance from the leading edge and in Figure 2 the pressure gradient is shown. The reference pressure is taken at x=450 mm in the non-diverging part of the flow.

The pressure distribution is shaped as Schubauer and Spangenberg (1960) suggested, with an initially steep and progressively decreasing gradient to get an optimal pressure recovery. At the early stage of the pressure rise the thin boundary layer can withstand a stronger gradient. When the pressure acts on the boundary layer the wall shear stress is decreasing rapidly and the boundary layer grows

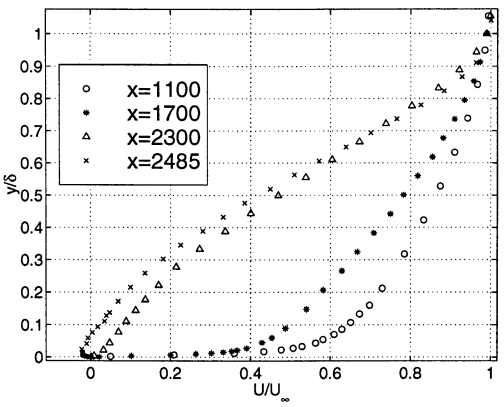

Figure 3: Mean velocity profiles

fast and becomes more sensitive.

The spanwise non-uniformity was at most a couple of percent.

BOUNDARY LAYER DEVELOPMENT

The boundary layer development was measured using single component LDV. The flow was seeded by means of a smoke generator using glycol. Measurements were carried out for the streamwise (U) component at x=1100, x=1700 x=2300, x=2485, see straight lines in Figure 1 and 2.

Mean profiles

Figure 3 shows the down stream development of the stream wise U component scaled with the local free stream value and plotted against the wall normal coordinate scaled with the boundary layer thickness. The boundary layer development in terms of the integral scales is shown in Table 1. The characteristic rapid thickening due to the APG and the increase in shapefactor is evident.

The first x-position at x=1100 shows a typical ZPG profile with a well defined log region. The shape factor H_{12} is 1.4 which is the ZPG value at Re_θ=4000, see Österlund (1999). At higher Re_θ, approximately 20000-25000, the value common in ZPG H_{12}=1.3 is approached.

At x=1700 the free stream velocity has changed from 26.49 m/s to 22.63 m/s and the profile starts to loose its fullness due to the APG. The shape factor H_{12} has only increased to 1.62 despite the fact that the largest pressure gradient is around x=1500 mm.

At x=2300 the strong APG effect has made the velocity profile loose its fullness. The logarithmic region has disappeared and the classical inner-outer description is no longer valid. A significantly larger rise from H_{12}=1.62 to H_{12}=3.33 in the same distance as between the

x(mm)	U_∞(m/s)	δ(mm)	δ^*(mm)
1100	26.49	19	3.28
1700	22.63	34	8.45
2300	17.76	91	46.29
2485	17.20	115	62.82
x(mm)	θ(mm)	H_{12}(mm)	Re_θ
1100	2.31	1.42	4093
1700	5.21	1.62	7865
2300	13.92	3.32	16505
2485	15.23	4.12	17500

Table 1: LDV measurement parameters

two former positions despite the fact that the pressure gradient is relaxed. This illustrates the fact that a thin boundary layer can withstand an initially steep gradient as stated by Schubauer and Spangenberg (1960).

At x=2485 a well defined region of mean reverse flow can clearly be seen close to the plate.

Wall shear stress

The mean wall shear stress was measured with Preston tubes up to x=2150.

Clauser plots can also be used to determine the friction velocity i.e. the wall shear stress as long as there exists a well defined two-layer structure with a logarithmic region. This is the case at x=1100 and x=1700.

Additional LDV measurements were made close to the wall in the viscous sublayer where the velocity gradient is small. At x=2300 and x=2320 the wall shear stress was determined by a linear least squares fit to three measurement points extrapolated to the wall using the no-slip condition. The wall shear stress has almost vanished and the flow is close to separation.

Figure 4 shows a comparison of the different wall shear stress measurements. The agreement is fair and the decrease in wall shear stress due to the APG is evident. The wall shear stress decreases rapidly in the beginning of the pressure rise when the shape factor is only slightly changed.

Turbulence statistics

In Figure 5 the first x-position at x=1100 shows a typical ZPG u_{rms} profile with the near wall peak close to the wall.

The second x-position at x=1700 shows the typical feature of APG boundary layers. The inner peak has not yet disappeared but a new APG induced maxima starts to develop further out in the flow around y/δ^*=1 where the mean velocity profile has its inflection point giving the largest gradient and maximum shear.

Further downstream, at x=2300 and

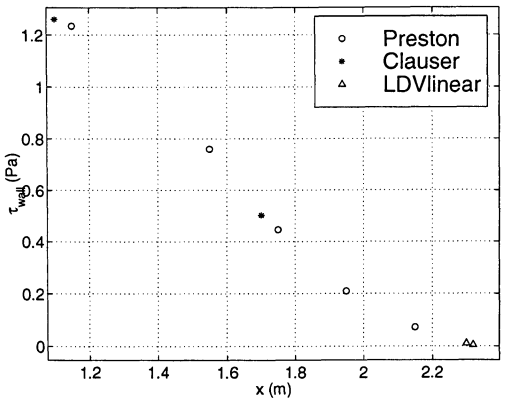

Figure 4: Mean wall shear stress measurements

x=2485, the u_{rms} peak close to the wall has disappeared but the new maxima is still located around y/δ^*=1. This position scales with δ^* but not with δ indicating the significance of δ^* for scaling.

Figure 6 shows the u_{rms} profiles in inner variables using the wall shear stress data to get the friction velocity. The peak at x=1100 is located at about y^+=20 in the buffer region.

At x=1700 the near wall peak is still left and the new APG maxima is developed at about y^+=400.

At x=2300 the peak is closer to y^+=300 but the exact position is very uncertain due to uncertainties in the determination of the viscous length scale when the wall shear stress is about to vanish. It seems like the position of the maxima is fix also in viscous scaling at about y^+=300-400 indicating that there is only one length scale governing the APG flow since the ratio between the inner and the outer scale is independent of the development of the boundary layer.

MEASUREMENTS NEAR AND IN THE SEPARATED REGION

PIV measurements were done at five different x-positions in the wall normal xy-plane between x=2280 mm and x=2763 mm including the position of separation and reattachment.

Table 2 shows integral parameters from integrated PIV measurements that reach out to the free stream. H_{12} is approximately constant around 4 in the entire separated region between x=2490-2627 and the integral length scales grow linearly in the downstream direction i.e. the shear-layer is in "equilibrium".

H_{12} in this case characterizes the shear-layer above the shallow separation bubble, which appears to be rather unaffected by the backflow underneath.

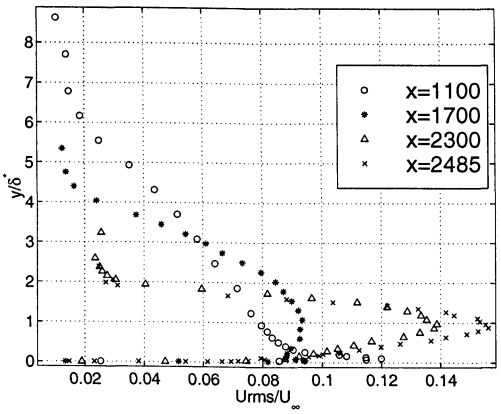

Figure 5: u_{rms} velocity profiles

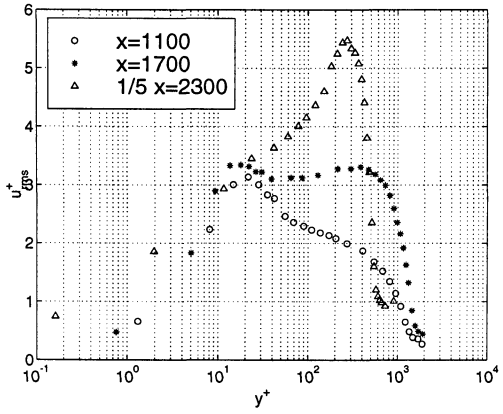

Figure 6: Fluctuating velocity in inner variables for x=1100 mm, x=1700 mm and x=2300

The value of the shape factor H_{12} at separation is less than 3.98 and above 3.33 according to the LDV data. This is slightly larger than the values reported earlier by Dengel and Fernholz (1990) 2.85±0.1, Muhammad-Klingmann and Gustavsson (1999) 3.25±0.15 (at reattachment) and Holm and Gustavsson (1999) 3.4±0.3.

Mean velocity scaling

Perry and Schofield (1973) developed a velocity defect scaling

$$\frac{U_\infty - U}{u_s} = f(\frac{y}{B}) \qquad (2)$$

that is not based on u_τ, but introduces another velocity scale u_s, and a corresponding outer length scale,

$$B = 2.86\delta^* \frac{U_\infty}{u_s} \qquad (3)$$

similar to Clausers outer length scale Δ.

u_s is related to maximum shear which seems reasonable since the wall shear stress in ZPG is the maximum shear which determines u_τ.

According to Schofield (1981) u_s can be determined in a similar manner to u_τ from a Clauser plot but using a half-power law instead of the log-law.

Schofield (1981) verified this scaling in equilibrium boundary layers and Schofield (1986) showed that it is valid after separation as well.

More recently Dengel and Fernholz (1990) claimed that a 7^{th} order polynomial was found to give a better fit to their data than the original profile. They also found a correlation between the velocity scale u_s and χ_w, the amount of time the flow spends in the upstream direction. This was used here to determine u_s.

Figure 7 shows PIV data at x=2490, x=2540, x=2570 and x=2627 (above the thin bubble where the flow is separated) scaled with these coordinates. The collapse of the present data is excellent even though the present data do not fit the original profile nor the one suggested by Dengel and Fernholz (1990). Hence, there seems to be a self-similarity, but the exact shape of the profile differs from case to case.

Reynolds stresses

Figure 10 shows the downstream development of the Reynolds stresses. Velocities are extracted from the 5 different PIV measurements and an average over 6 pixels is made at all positions.

The maximum in the Reynolds stresses increase linearly in the down stream direction like in the case of Dengel and Fernholz (1990). This is most pronounced in u_{rms}. When scaled with the maximum value which must be related to the maximum shear and plotted against y/δ^*, there seem to be similarity.

The maximum in all the Reynolds stresses are located at approximately y/δ^*=1, i.e. the same position as was seen in the LDV data, where the mean velocity profile has an inflection point. This is also the position of maximum in turbulent production. This position is equivalent to y/δ=0.55 in the present case which is similar to what Dengel and Fernholz (1990) reported. Skåre and Krogstad (1994) reports a value of y/δ=0.45 for H_{12}=2 which shows that the position of the new APG maxima moves further out, in terms of y/δ, as consequence of the rise in H_{12} but not in terms of y/δ^*. Independent of a change in H_{12}=1.62-4.12 i.e. without the restriction of equilibrium, the position of maxima scales with δ^*.

$$R_{uv} = \frac{\overline{u'v'}}{u_{rms} v_{rms}} \qquad (4)$$

x(mm)	U_∞(m/s)	δ(mm)	δ^*(mm)
2280	-	-	-
2490	17.21	110	59.94
2540	17.19	113	63.23
2570	17.05	116	65.19
2627	17.02	119	67.79
2763	-	-	-
x(mm)	θ(mm)	H_{12}(mm)	Re_θ
2280	-	-	-
2490	15.05	3.98	17264
2540	15.75	4.01	18051
2570	16.23	4.02	18448
2627	16.77	4.04	19024
2763	-	-	-

Table 2: PIV measurement parameters

The maximum in the correlation coefficient R_{uv} $0.2 \leq y/\delta^* \leq 1.4$ is around 0.3-0.4 which is close to the ZPG boundary layer. The u and v components are well correlated in the middle of the layer and closer to the wall and the edge the correlation goes to zero. Despite the scatter it is clear that the correlation coefficient is self-similar throughout the separated region.

The structure parameter, i.e. the ratio of v_{rms} to u_{rms} shows that v_{rms} goes to zero faster than u_{rms} close to the wall, presumably because the wall suppresses fluctuations in the normal direction. At $0.1 \leq y/\delta \leq 0.55$ the ratio is approximately constant around 0.55-0.6. Skåre and Krogstad (1994) compared all the structure parameters to the ZPG case and noted that the pressure gradient does not have an effect on the ratios of the Reynolds stresses i.e. the mechanism for distributing the turbulent energy is not affected. This is also seen in the present data.

SUMMARY AND CONCLUSIONS

An experimental set-up was designed for a separating high Re turbulent APG boundary layer reaching Re_θ=19000.

A quasi-two-dimensional, steady and shallow separation bubble was investigated using PIV and 1-component Laser Doppler Velocimetry (LDV). Wall normal measurements were made prior to separation, inside and above the separation bubble and after reattachment. Experimental data such as boundary layer development, turbulence statistics, pressure gradient and mean wall shear stress are presented. The present data are in agreement with earlier experiments.

The shear-layer above the separated region is in "equilibrium" with a constant shape factor H_{12}=4 and linearly growing integral scales δ, δ^*, θ. The magnitudes of the maxima in the Reynolds stresses are also linearly increasing in the down stream direction as was also found by

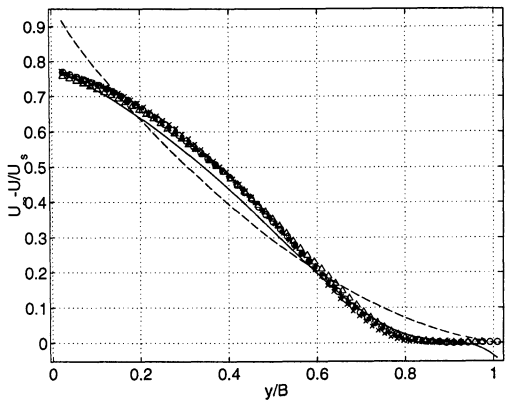

Figure 7: Scaling according to Perry and Schofield (1973) (dashed line) and Dengel and Fernholz (1990) (full line) for PIV data at x=2490-2627

Dengel and Fernholz (1990).

The mean profiles were shown to be self-similar when scaled with the Perry-Schofield coordinates using the linear relation between the velocity scale u_s and χ_w found by Dengel and Fernholz (1990).

The Reynolds stresses are also self-similar when scaled with their maximum value and plotted against y/δ^*. The maximum in all the Reynolds stresses is located at y/δ^*=1 which coincides with the position of maximum shear i.e. the inflection point of the mean velocity profile. Measurements well upstream of separation show that this is also true in a large range of H_{12} where the flow is not in equilibrium, H_{12}=1.62-4.12, i.e. the position of the new APG maxima is insensitive to the development of the boundary layer. Upstream of separation y/δ^*=1 corresponds to approximately y/l_*=400 *at all x−positions*, i.e. there is a constant ratio between the inner and outer scales, indicating that there is only one length scale governing the flow. This is equivalent to a constant Reynolds number based on δ^* and u_τ.

$$Re = \frac{u_\tau \delta^*}{\nu} = 400 \qquad (5)$$

There is no longer an inner and outer region and the classical two-layer structure is not a valid description of the boundary layer. The logarithmic overlap region disappears when backflow occurs according to Dengel and Fernholz (1990). The importance of the inner region disappears when the wall shear stress decreases and the friction velocity is no longer the appropriate velocity scale. The new maxima in the Reynolds stresses is associated with the maximum shear and a velocity scale like u_s suggested by Perry and Schofield (1973) which is related to the maximum shear therefore seems

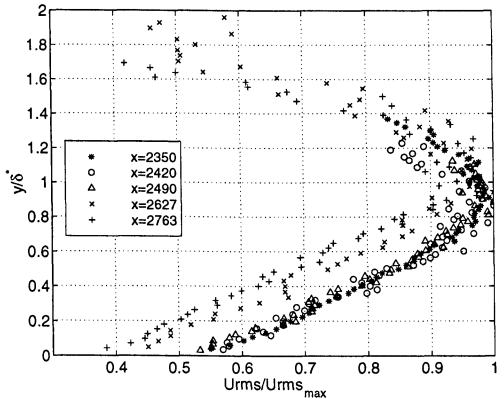

Figure 8: u_{rms}

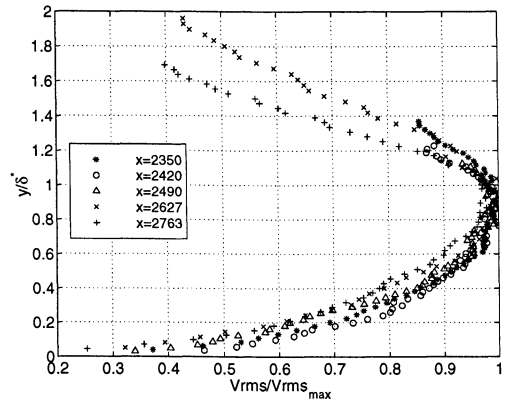

Figure 9: v_{rms}

reasonable. As stated by Skåre and Krogstad (1994), when scaling their Reynolds stresses, they might as well have used the maximum shear instead of u_τ.

References

Dengel, P. and Fernholz, H., 1990, "An experimental investigation of an incompressible turbulent boundary layer in the vicinity of separation", *Journal of Fluid Mechanics*, Vol. 212, pp. 615-636.

Holm, R. and Gustavsson, J., 1999 "A PIV study of separated flow around a 2D airfoil at high angles of attack in a low speed wind tunnel", FFA TN 1999-52.s

Lindgren, B. 1999, "Development of guide-vanes for expanding corners with application in wind-tunnel design", Licentiate Thesis 1999:08, Dept. of Mechanics, Royal Institute of Technology, Stockholm.

Muhammad-Klingmann, B. and Gustavsson, J., 1999, "Experiments on turbulent flow separation", *IMechE C557/153/99.*

Perry, A. and Schofield, W., 1973, "Mean velocity and shear stress distribution in turbulent boundary layers" ,*Physics of Fluids*, Vol. 113, pp. 2068-2074.

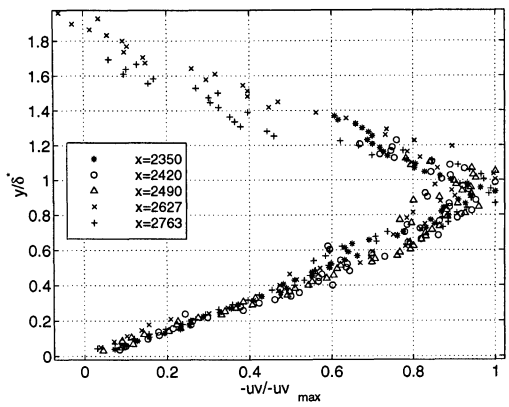

Figure 10: Re shear stress

Schofield, W., 1981, "Equilibrium boundary layers in moderate to strong adverse pressure gradient", *Journal of Fluid Mechanics*, Vol. 113, pp. 91-122.

Schofield, W., 1986, "Two-dimensional separating turbulent boundary layers", *AIAA Journal*, Vol. 24 (10), pp. 1611-1619.

Schubauer, G. and Spangenberg, W., 1960, "Forced mixing in boundary layers", *Journal of Fluid Mechanics*, Vol. 8, pp. 10-32.

Skåre, P. and Krogstad, P., 1994, "A turbulent equilibrium boundary layer near separation", *Journal of Fluid Mechanics*, Vol. 272, pp. 319-348.

Österlund, J., 1999, "Experimental Studies of Zero Pressure-Gradient Turbulent Boundary-Layer Flow", Doctoral Thesis 1999:16, Dept. of Mechanics, Royal Institute of Technology, Stockholm.

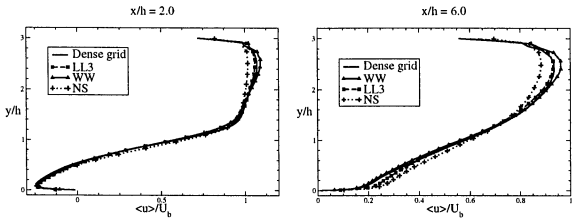

Figure 11: Distribution of streamwise velocity with the WALE model for 3 wall-treatments and the medium grid.

point, in which case, sensitivy to SGS and near-wall modelling is very high. As resolution improves, this sensitivity declines and resonable agreement with the highly-resolved solution is obtained. Although none of the simulations is satisfactory, those using Werner-Wengle wall-law and the WALE model models are found to give results closest to the highly-resolved simulation.

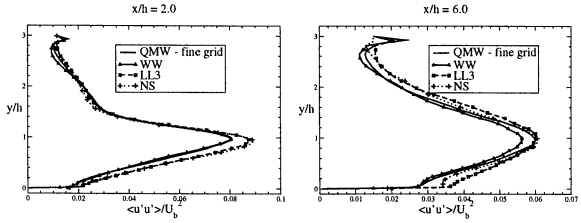

Figure 12: Distribution of streamwise stress with the WALE model for 3 wall-treatments and the medium grid.

CONCLUSIONS

The study has demonstrated that the simulation of separation from curved surfaces can be very sensitive to the grid density, the details of the near-wall treatment and the nature of the SGS model. This sensitivity appears to be rooted, principally, in variations of the predicted separation point: a small downstream shift of this point leads to a major shortening of the recirculation region and major changes in gross flow features. In the present flow, sensitivity seems to be especially pronounced because of the periodic nature of the flow and because the boundary layer is subjected, prior separation, to large rates of streamwise straining, and thus structural changes.

Of the practices examined, the combination of the WALE SGS model, giving low levels of SGS viscosity, and Werner-Wengle near-wall approximation is the most effective in returning the closest fidelity to the highly-resolved solution. *A-priori* tests show that the true near-wall flow does not adhere well to the assumptions underpinning any of the wall-laws used. Thus, better near-wall treatments are imperative if the physical realism of coarse-grid simulations is to be improved.

ACKNOWLEDGMENTS

This work is part of the LESFOIL project (No. BRPR-CT97-0565), financed through the Brite-Euram programme.

REFERENCES

Almeida, G.P., Durão, D.F.G., and Heitor, M.V., 1993, *Experimental Thermal and Fluid Science*, Vol. 7, pp. 87-101.

Balaras, E., Benocci, C., and Piomelli, U., 1996, *AIAA Journal*, Vol. 34, pp. 1111-1119.

Cabot, W., and Moin, P., 1999, *Flow, Turbulence and Combustion*, Vol. 63, pp. 269-291.

Dahlström, S., and Davidson, L., 2000, *Proceedings, ECCOMAS 2000.*

Germano, M., Piomelli, U., Moin, P., and Cabot, W.H., 1991, *Physics of Fluids A*, Vol. 3 , pp. 1760-1765.

Grötzbach, G., 1987, *Encyclopedia of Fluid Mechanics*, Vol. 6, pp. 1337-1391.

Le, H., Moin, P., and Kim, J., 1997, *Journal of Fluid Mechanics*, Vol. 330, pp. 349-374.

Lilly, D.K., 1992, *Physics of Fluids A*, Vol. 4, pp. 633-635.

Mansour, N.N., Kim, J., and Moin, P., 1988, *Journal of Fluid Mechanics*, Vol. 194, pp. 15-44.

Mellen, C.P., Fröhlich, J., and Rodi, W., 2000, *Proceedings, 16th IMACS World Congress.*

Moser, R.D, Kim, J and Mansour, N.N, 1999, *Physics of Fluids*, Vol. 11, pp. 943-945.

Murakami, S., Mochida, A., Rodi, W., and Sakamoto, S., 1993, *ASME FED, Engineering applications of large eddy simulations*, Vol. 162, pp. 113-120.

Nicoud, F., and Ducros, F., 1999,*Flow, Turbulence and Combustion*, Vol. 62, pp. 183-200.

Piomelli, U., and Liu, J., 1995, *Physics of Fluids*, Vol. 7, pp. 839-848.

Sagaut, P., 1996, *La Recherche Aérospatiale*, Vol. 1, pp. 51-63.

Smagorinsky, J., 1963, *Monthly Weather Review*, Vol. 91, pp. 99-163.

Spalart, P.R., Jou, W-H., Strelets, M., and Allmaras, S.R., 1997, *Proceedings, Advances in DNS/LES.*

Temmerman, L., Leschziner, M.A., Ashworth, and Emerson, D.R., 2000, ,*Proceedings, Parallel CFD 2000.*

Werner,H., and Wengle, H., 1991, *Proceedings, 8th Symposium on Turbulent Shear Flows*, pp. 155-168.

NUMERICAL INVESTIGATION OF THE SEPARATED FLOW OVER A SMOOTHLY CONTOURED RAMP

Bono Wasistho*
Mechanical and Aerospace Engineering Department
Arizona State University
Tempe, Arizona 85287-6106, USA
wasistho@galileo.cse.uiuc.edu

Kyle D. Squires
Mechanical and Aerospace Engineering Department
Arizona State University
Tempe, Arizona 85287-6106, USA
squires@asu.edu

ABSTRACT

Large Eddy Simulation (LES) and Reynolds-averaged Navier-Stokes (RANS) calculations have been used to predict the development, separation, reattachment and downstream recovery of the flow over a smoothly contoured ramp. The statistically two-dimensional upstream flow separates along the ramp surface and then reattaches downstream on a flat section. A canonical flat-plate turbulent boundary layer at a momentum thickness Reynolds number 1100, and having a boundary layer thickness $0.13L_r$, is introduced four ramp lengths upstream of the onset of curvature. Subgrid-scale (SGS) stresses in the LES are closed using the dynamic eddy viscosity model of Germano *et al.* (1991). RANS calculations of the steady-state solution are performed using two leading models: Spalart-Allmaras (Spalart-Allmaras 1994) and v^2-f (Durbin 1991). Mean flow predictions obtained using all the models agree well with the experimental measurements of Song *et al.* (2000). Boundary layer detachment occurs along the curved section ($x/L_r \approx 0.4$) with reattachment at roughly $x/L_r \approx 1.4$. The primary turbulent shear stress sharply increases in the separated region and LES predictions of the shear stress development are accurate. RANS estimations of the shear stress are below the data in the separated region, though reasonable further downstream.

INTRODUCTION AND OBJECTIVES

Separated boundary layers are a challenging subset of flows that may be generally classified as 'non-equilibrium'. Non-equilibrium boundary layers are the norm, rather than the exception, in engineering applications. The importance of additional length scales to describing the flow and/or a significant imbalance between production and dissipation are two features which characterize these flows. An adverse pressure gradient boundary layer approaching separation develops an inflection point, the height of which is an additional important length scale. Turbulent stresses, for example, develop large peaks around the inflection point and boundary layer recovery following reattachment should be expected to be sensitive to this length scale.

These and other features of separated flows substantially challenge predictive methods. The vast majority of engineering predictions are obtained from solutions of the Reynolds-averaged Navier-Stokes (RANS) equations. In flows not far from equilibrium, the boundary conditions that define large scale structures remain nearly unchanged and the leading RANS models are typically adequate.

In separated flows, however, RANS models often yield mixed results (e.g., see Apsley and Leschziner 1999), providing one rationale for use of techniques such as Large Eddy Simulation (LES). In LES, the large, energy-containing scales of motion are resolved on the mesh and only the small, subgrid scales are modeled. LES predictions are less sensitive to modeling errors than their RANS counterparts. This feature should be an advantage in prediction of flows far from the calibration range of RANS models and in regimes with multiple perturbations (e.g., in pressure gradient, streamline curvature, roughness, etc.).

Assessment of simulation techniques for predicting separated boundary layers is complicated

*current address: Center for Simulation of Advanced Rockets, University of Illinois, Urbana, Illinois 61801, USA

by the fact that there is relatively strong coupling between the freestream and boundary layer. This in turn increases the sensitivity of the flow to parameters not directly connected to the turbulence model and may not allow one to easily isolate the cause of discrepancies between numerical simulation and experiment. Therefore, it is useful in any study directed towards refined evaluation of techniques and models that careful evaluation of a baseline case be established.

One of the overall aims in this work is prediction of the effect of Reynolds number on separated boundary layers (see also Song and Eaton 2001 in this volume). In the present contribution the flow at moderate Reynolds number is predicted using LES and RANS in order to assess the accuracy of each technique as well as to investigate some of the underlying characteristics of the flow. The particular flow under consideration is the statistically two-dimensional boundary layer which separates over a smoothly contoured ramp (Figure 1). The location of boundary layer detachment is not fixed by the geometry and the flow provides a reasonably well-defined platform for investigating the processes of reattachment and downstream recovery. Experimental measurements from Song *et al.* (2000) are used to evaluate the predictions.

SIMULATION OVERVIEW

The ramp geometry is shown in Figure 1. As shown in the figure, the origin of the coordinate system is fixed to the onset of the contoured section. The ramp is a portion of a circular arc in which the vertical extent is roughly one-third of the streamwise length, L_r. The reference boundary layer thickness measured upstream of the onset of curvature was about 13% of the ramp length. For other details of the experimental setup the reader is referred to Song *et al.* (2000).

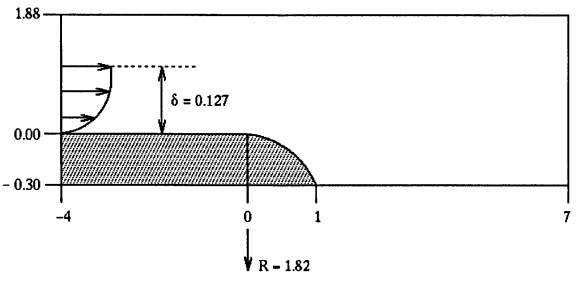

Figure 1: Ramp schematic. Curved section formed by a portion of a circular arc (note the enlarged vertical scale). Lengths in the figure and throughout have been non-dimensionalized by the ramp length L_r.

Experimental measurements are available at several streamwise locations, beginning at $x/L_r = -2$. As discussed in the next section (c.f., Figure 2), the downstream effects (pressure gradient and curvature) are already significant enough that prescribing an inflow signal in the simulations that did not exhibit an unphysical adjustment was difficult. Consequently, the simulation domain was extended two ramp lengths further upstream ($x_{in}/L_r = -4$) which was sufficient to ensure that inflow signals did not undergo arbitrary adjustment.

Predictions presented in this manuscript are obtained using Large Eddy Simulation (LES) and from the Reynolds-averaged Navier-Stokes (RANS) equations. In both approaches, an eddy viscosity hypothesis is used to close the subgrid-scale stress in the LES and Reynolds stress in the RANS. Two of the leading linear eddy viscosity models are employed in the RANS calculations: Spalart-Allmaras (referred to as 'S-A' throughout) (Spalart & Allmaras 1994) and $\overline{v^2}$–f (Durbin 1991). The dynamic Smagorinsky model is used in the LES (Germano *et al.* 1991).

In the dynamic model an expression is derived for the model coefficient via application of a "test filter" to the resolved field (applied at a scale twice as large as the grid scale). An expression for the model coefficient can be derived and evaluated during the course of the simulation. The advantage of this approach is that the model coefficient is not specified *a priori*, but rather is sensitive to local variations in the flow. On the other hand, the expression for the model coefficient can be ill-conditioned and requires spatial averaging over the statistically homogeneous spanwise direction to maintain numerical stability. Negative values of the model coefficient imply a backscatter of energy from the subgrid to resolved scales of motion and are accounted for in the dynamic procedure, albeit in an average sense. To avoid numerical instability, negative values of the subgrid viscosity were truncated to zero.

The numerical approach is based on solution the incompressible Navier-Stokes equations using a fractional step method (e.g., see Choi *et al.* 1993, Wu and Squires 1998). The present calculations are "2.5D", i.e., a curvilinear geometry in the x-y plane but with a uniform spanwise (z) coordinate along which periodic boundary conditions are applied. The homogeneous spanwise coordinate improves statistical sample, but does introduce the spanwise period as a parameter of the calculation. In the present simulations, the spanwise domain length is $4\delta_{in}$ where δ_{in} is the boundary layer thickness at the inflow plane. Two-point correlations showed this spanwise period is adequate.

The LES calculations were performed using a grid of 484 × 60 × 101 mesh points in the streamwise, wall-normal, and spanwise directions, re-

spectively. The RANS grid was 323 × 53 and refinement studies showed this is sufficient, yielding less than a 2% change in the peak skin friction compared to runs on a mesh coarser by a factor of two compared to the one used to obtain the results presented here. Partial grid refinement was also conducted in the LES, though an exhaustive study with sufficient time sampling to allow a thorough evaluation of grid-size effects was not possible.

In the calculations a statistically two-dimensional turbulent boundary layer is introduced at $x_{in}/L_r = -4$, corresponding to roughly 30 inflow boundary layer thicknesses (c.f. Figure 1). The LES inflow condition was prescribed using the technique developed by Lund *et al.* (1998). In this approach, an auxiliary simulation is performed of a canonical flat-plate boundary layer, with the results at a specified plane stored for subsequent use in the ramp calculation.

As discussed further in the next section, a shallow separation occurs in the curve with reattachment in the vicinity of $x/L_r = 1.4$. From the merger of the curved and downstream flat sections, the computational domain extends $6L_r$ downstream in the LES, slightly longer in the RANS. The vertical dimension of the computational domain was the same as that in the experiments. In the LES, a zero stress condition is applied along this boundary, while in the RANS the boundary layer was resolved along the upper wall. The LES therefore does not account for the blockage from the upper wall, which affects predictions of the pressure distribution (c.f., Figure 2).

At the exit plane of the computational domain ($x/L_r = 7$) a convective boundary condition was used, identical to that employed in related studies (e.g., see Wu and Squires 1998). The grid was generated using the direct grid distribution control technique of Thomas and Middlecoff (1980).

Calculations are performed for a momentum thickness Reynolds number, Re_θ, in the boundary layer at the inlet plane of 1100. This Reynolds number permits direct resolution of the wall layer in the LES with grid spacings fine enough to minimize modeling errors. The streamwise grid spacing in the LES is less than 80 wall units, the spanwise spacing is about 25 wall units (based on the friction velocity at the inflow boundary). These grid spacings are commensurate with related applications of LES to complex boundary layers which also resolved the wall layer (e.g., see Kaltenbach *et al.* 1999). SGS modeling errors are small (peak model stress contributions are everywhere less than 10% of the resolved stress). Because the LES is well resolved the calculation database provides a detailed description of the flow which complements the experimental measurements and also permits detailed evaluation of the RANS predictions.

RESULTS

The pressure and skin friction coefficients along the lower wall from Song *et al.* (2000), along with the simulation results are shown in Figure 2 and Figure 3, respectively. From about $x/L_r = -2$, the pressure gradient is first favorable due to streamline curvature with the minimum in C_p measured and predicted just downstream of the onset of the curved section. The minimum C_p is not as deep in the LES with the slip condition applied along the upper wall, whereas both RANS models, with no-slip upper walls, provide accurate predictions. Downstream of $x/L_r = -2$, the skin friction in Figure 3 responds to the curvature by increasing from its inlet value with the maximum attained near the onset of the ramp.

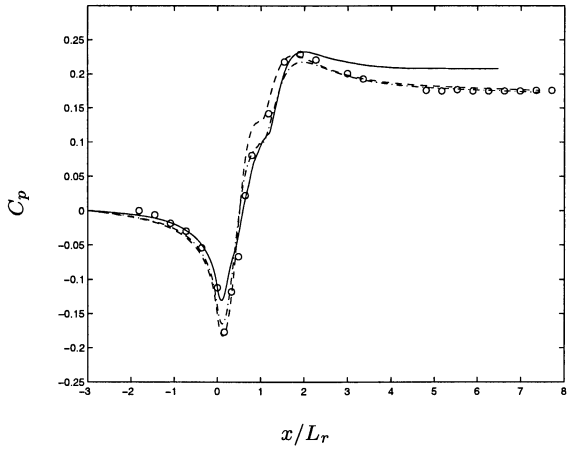

Figure 2: Pressure coefficient. ——— LES; - - - - S-A; —·— $\overline{v^2}$–f; o Song *et al.* (2000).

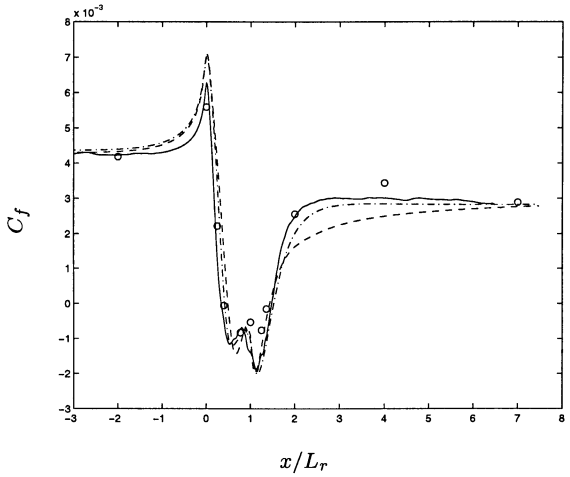

Figure 3: Skin friction coefficient. ——— LES; - - - - S-A; —·— $\overline{v^2}$–f; o Song *et al.* (2000).

The pressure gradient subsequently becomes strongly adverse and Figure 3 shows separation in

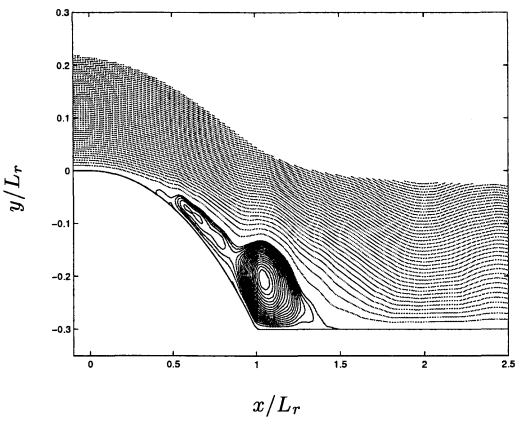

Figure 4: Streamlines in the vicinity of the recirculating region. Note the expanded vertical scale.

the mean at $x/L_r \approx 0.4$. The LES and RANS yield similar predictions of the separation location with slightly earlier detachment found in the LES. The two C_f minima in the separated region and behavior in C_p around $x/L_r = 1$ are related to the structure of the separated region. Streamlines in the vicinity of the separation zone in Figure 4 show that the reverse-flow region is comprised of two main recirculating motions: a primary recirculation at the merger of the curved and flat sections and a smaller secondary zone upstream.

Figure 3 shows that reattachment in the mean takes place around $x/L_r \approx 1.4$. In general, LES predictions of the skin friction are in the most favorable agreement with measurements in the recovery region, with the RANS predictions exhibiting a slower recovery in C_f. Note also that the downstream values of C_p are over-predicted in Figure 2, again showing the influence of the upper-wall boundary condition. Though not shown here, RANS predictions using no-stress conditions along the upper surface yield C_p distributions nearly the same as the present LES.

Figure 5 shows the time history of the separation and reattachment positions (averaged over the spanwise dimension). Fluctuations in the separation position occur at higher frequencies and exhibit smaller streamwise variations than the lower frequency observed in the reattachment location. Both the separation and reattachment trajectories in Figure 5 indicate that the separation/reattachment process is inherently unsteady and characterized by rather abrupt shedding events. Contours of the vorticity magnitude in curvilinear planes shown in Figure 6 provide another view of the flow. Close to the wall (top frame, $y/\delta_{in} = 0.018$) the vorticity field is stretched in the streamwise direction with the contours becoming more isotropic within the recirculation region and then recovering the elongated shape further downstream. This behavior is still apparent at the mid-position (middle frame, $y/\delta_{in} = 0.08$). The (curvilinear) plane at $y/\delta_{in} = 0.26$ shows significantly more activity in the vorticity field downstream of separation than in either of the planes closer to the wall. Thus, while Figure 5 provides evidence that the separation and reattachment processes are characterized by 'periodic' sheddings, Figure 6 indicates that there does not appear to be a structure of considerable spanwise coherence that dominates the separation process.

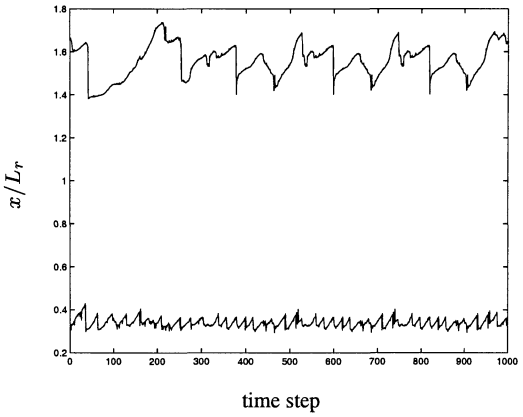

Figure 5: Temporal development of the separation and reattachment locations in the LES.

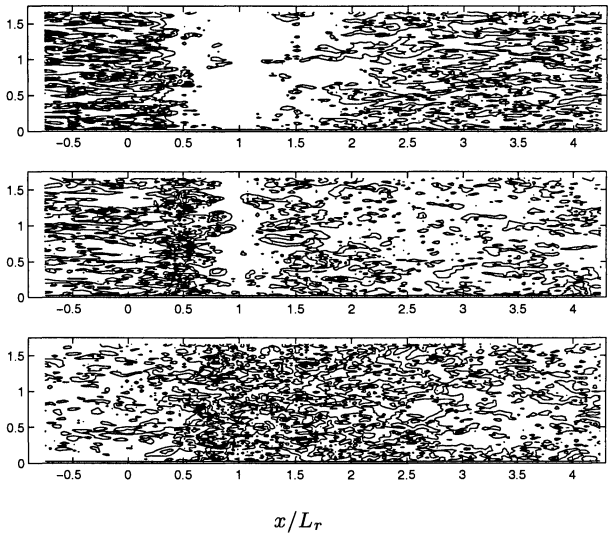

Figure 6: Contours of the vorticity magnitude in curvilinear planes $y/\delta_{in} = 0.018$ (top frame), 0.08 (middle frame), and 0.26 (bottom frame) where δ_{in} is the boundary layer thickness at the inflow plane.

Profiles of the streamwise mean velocity are shown in Figure 7. The upper frame shows profiles covering the entire streamwise extent of the calculation while the lower frame shows measurements and simulation results in the vicinity of the separation region. In general, the figure shows that both LES and RANS predictions of the mean streamwise flow are in good agreement with the measurements of Song *et al.* (2000). Boundary layer deceleration and separation are accurately predicted, as already discussed in reference to Figure 3. The

lower frame in Figure 7 provides an illustration of the relatively shallow nature of the separation. The peak backflow velocity is on the order of 10% of the freestream value and is well predicted by all the simulations. While the region of reversed flow is relatively shallow, the perturbation applied by boundary layer detachment/reattachment is relatively strong. Though not obvious from the figure, the mean profile at the furthermost streamwise position, $x/L_r = 7$ (≈ 45 inlet boundary layer thicknesses from the reattachment location), has not yet recovered the logarithmic law.

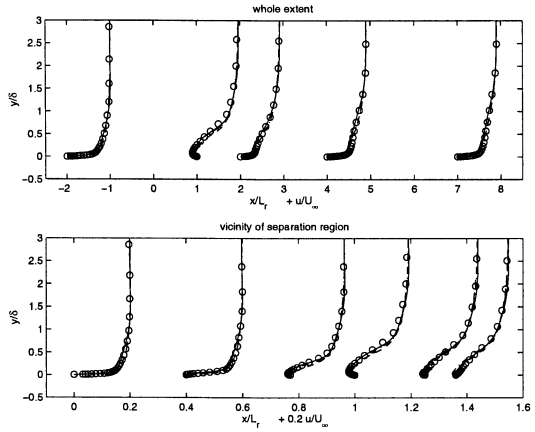

Figure 7: Mean streamwise velocity. ——— LES; - - - - S-A; —·— $\overline{v^2}$–f; ○ Song *et al.* (2000).

Shown in Figure 8 are predictions of the turbulent shear stress from the LES and RANS, compared to the experimental measurements of Song *et al.* (2000). As with the mean flow, the upper frame shows the entire streamwise extent while the lower frame focuses on the profiles in the separation region. At $x/L_r = 0.25$, the adverse pressure gradient has raised the peak shear stress compared to the inlet value with all the simulations accurately predicting the profile. In the reverse flow region the peak shear stress increases further, with its peak shifted from the wall, characteristic of adverse pressure gradient and separated boundary layers (e.g., see Simpson 1989). Note that while the shear stress levels are accurately predicted in the LES, Figure 8 shows that the RANS predictions underestimate the shear stress by about a factor of two. Though not shown here, the underestimation is linked to relatively low eddy viscosity levels in the RANS (nearly a factor of five smaller towards the downstream stations).

One view of the distortion and recovery process is shown in Figure 9. Plotted is the downstream development of the streamwise fluctuating velocity. In Figure 9a the adverse pressure gradient raises the velocity fluctuation with the peak value also further from the wall. The profiles in Figure 9b are within the reverse-flow region and then also in the

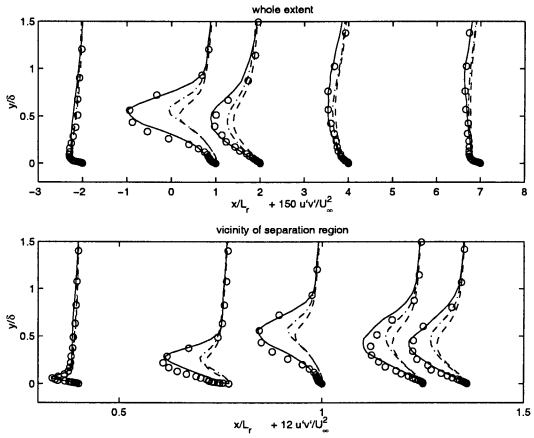

Figure 8: Primary turbulent shear stress. ——— LES; - - - - S-A; —·— $\overline{v^2}$–f; ○ Song *et al.* (2000).

recovery region following reattachment. The reattaching boundary layer recovers through growth of an inner layer (evident by $x/L_r = 2$) as well as through decay of the elevated stress levels in the outer region. As commented previously in relation to the mean flow, Figure 9 shows that by $x/L_r = 7$ the fluctuating velocity has not yet recovered to its upstream state. Thus, the recovery process is comprised of two mechanisms: development and growth of an inner layer following reattachment and decay of elevated stress levels in the outer layer.

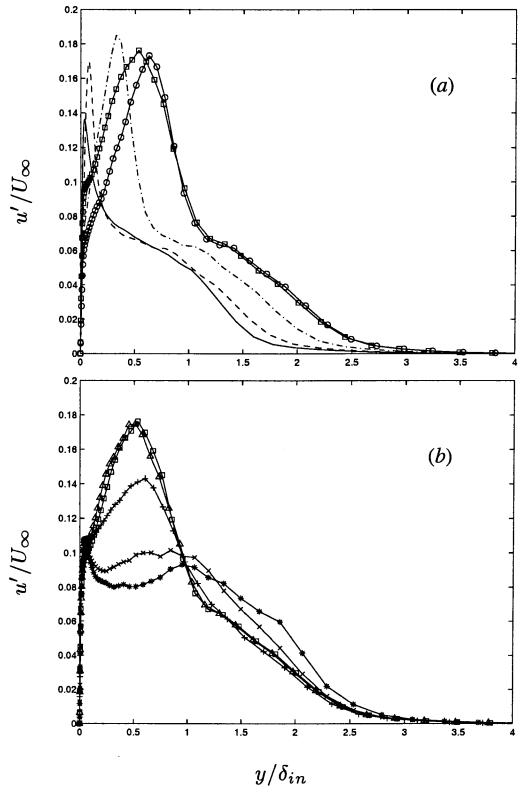

Figure 9: Development of streamwise velocity fluctuations. (*a*) x/L_r : ——— −2.00; - - - - 0.00; —·— 0.40; ○ 0.77; □ 1.00. (*b*) x/L_r : □ 1.00; △ 1.25, + 2.00; × 4.00, ∗ 7.00.

SUMMARY

Large eddy simulation and Reynolds-averaged Navier-Stokes calculations have been applied to prediction of the spatial development, separation, reattachment and downstream recovery of the boundary layer over a smoothly contoured ramp. Overall, there is fairly good agreement between LES and RANS predictions of the mean flow and the measurements of Song *et al.* (2000).

The flow exhibits a shallow separation with the region of reverse flow about one ramp length. Time series from the LES indicate that both the separation and reattachment are characterized by (time-dependent) shedding events. This inherently unsteady feature is resolved in the LES, but is difficult to parameterize within RANS closures. That difficulty is part of the explanation for the low shear stress predictions by the RANS models, especially in the reverse-flow region (c.f., Figure 8). RANS eddy viscosity levels lagged those of the LES solutions, indicative of lower mixing in the RANS calculations. Unsteady shedding of structures from the ramp into the zone of reverse flow should enhance mixing and are also an explanation for the lag in recovery of the skin friction (c.f., Figure 3). In addition, the Boussinesq approximation, applied in both the LES and RANS, becomes less reliable as separation is approached and as the boundary layer subsequently detaches with the flow departing far from equilibrium. Given the moderate Reynolds number and relatively fine mesh resolutions the modeling error in the subgrid closure has a small effect in the LES. In the RANS predictions, however, the error is substantially greater since the turbulence model dominates the solution.

The current calculation was performed at moderate Reynolds number in order to resolve the near-wall flow and avoid the empiricism that appears inevitable with wall-layer modeling for high Reynolds number LES applications. At the substantially higher Reynolds numbers representative of applications, and for which measurements are available, it appears unavoidable that LES can be applied without also introducing more empirical input (such as the law-of-the-wall in a wall-layer model, for example). The separation between the length scale characterizing the inflection of the velocity profile and near-wall structures is substantial at high Reynolds numbers and turbulence models will need to be responsive to such effects.

Acknowledgments

This work was supported by the U.S. Office of Naval Research (Grant Number N00014-98-1-0060, Program Officers: Dr. L. Patrick Purtell and Dr. Candace Wark). The authors gratefully acknowledge valuable discussions with Professor John Eaton, Dr. Philippe Spalart, and Mr. Simon Song. The simulations were performed on the Cray J90 at the U.S. Department of Defense High Performance Computing Major Shared Resource Centers (CEWES and NAVO).

REFERENCES

Apsley, D.D., and Leschziner, M.A., 1999, "Advanced turbulence modeling of separated flow in a diffuser", *Flow, Turbulence and Combustion*, **63**, pp. 81-112.

Choi, H., Moin, P., and Kim, J., 1993, "Direct numerical simulation of turbulent flow over riblets", *J. Fluid Mech.*, **255**, pp. 503-539.

Durbin, P.A., 1991, "Near-wall turbulence closure without damping functions", *Theo. and Comp. Fluid Dynamics*, **3**, pp. 1-13.

Germano, M., Piomelli, U., Moin, P. & Cabot, W.H., 1991, "A dynamic subgrid-scale eddy viscosity model", *Phys. Fluids*, **3**, p. 1760.

Kaltenbach, H.-J., Fatica, M., Mittal, R., Lund, T.S., and Moin, P., 1999, "Study of flow in a planar asymmetric diffuser using large-eddy simulation", *J. Fluid Mech.*, **390**, pp. 151-185.

Lund, T.S., Wu, X., and Squires, K.D., 1998, "Generation of turbulent inflow data for spatially-developing boundary layer simulations", *J. Comp. Physics*, **140**(2), pp. 233-258.

Simpson, R.L., 1989, "Turbulent boundary layer separation", *Ann. Review of Fluid Mechanics*, **21**, pp. 205-234.

Spalart, P.R. and Allmaras, S.R., 1994, "A one-equation turbulence model for aerodynamic flows", *La Recherche Aerospatiale*, **1**, pp. 5-21.

Song, S., DeGraaff, D., and Eaton, J.K., 2000, "Experimental study of a separating, reattaching and redeveloping flow over a smoothly contoured ramp", *Int. J. Heat and Fluid Flow*, **21**(5), pp. 512-519.

Thomas, P.D., and Middlecoff, J.F., 1980, "Direct control of the grid point distribution in meshes generated by elliptic equations", *AIAA J.*, **18**, pp. 652-656.

Wu, X., and Squires, K.D., 1998, "Numerical investigation of the turbulent boundary layer over a bump", *J. Fluid Mech.*, **362**, pp. 229-271.

MULTIPOINT MEASUREMENT OF WALL PRESSURE FLUCTUATIONS IN A SEPARATED AND REATTACHING FLOW OVER A BACKWARD-FACING STEP

Inwon Lee*
Department of Mechanical Engineering, KAIST
305-701 Taejon, Korea
s_liw@kaist.ac.kr

Hyung Jin Sung
Department of Mechanical Engineering, KAIST
305-701 Taejon, Korea
hjsung@kaist.ac.kr

ABSTRACT

Time-dependent characteristics of wall pressure fluctuations in separated and reattaching flows over a backward-facing step were investigated by means of continuous wavelet transform. Emphasis was placed on the combination of time-localized analyses of wavelet transform and multi-point measurements of pressure fluctuations. Synchronized wavelet maps revealed the evolutionary behavior of pressure fluctuations and gave further insight into the modulated nature of large-scale vortical structures. It was found that there exist two modes of shed vortices: one is the global oscillation and the other is the vortex convection. The two alternating modes are synchronized with the flapping frequency component of pressure fluctuations. Toward the investigation of the direct relationship between the flow field and the relevant spatial mode of the pressure field, a new kind of wavenumber filtering of pressure distribution, termed as a spatial box filtering (SBF), is introduced and examined. The conditional averaged velocity time history reveals that this SBF mode, tuned with the length scale of large-scale vortical structure, suggests its usefulness in capturing the large-scale coherent vortical structure.

INTRODUCTION

In a recent paper by the authors (Lee and Sung 2001, hereinafter referred to as LS), the spatial and spectral statistics of pressure fluctuations in separated and reattaching flows over a backward-facing step were reported. Multi-point measurements with an array of microphones in the streamwise and spanwise directions provided a comprehensive data file pertaining to the spatial characteristics of pressure fluctuations in the frequency domain. The coherence and wavenumber spectra exemplified the convective features which are closely associated with the large-scale vortical structures in the separated shear layer. The streamwise wavenumber spectra in LS, together with a preliminary calculation of the space-time cross-correlation, indicated the existence of a stationary mode and the scale variations of shed vortices. These suggested a modulated, intermittent spatio-temporal structure of shear layer under the flapping motion. A literature survey reveals that many studies have been made to find the mechanism of flapping motion in separated and reattching shear layers (Eaton and Johnston 1982, Kiya and Sasaki 1985, Le et al. 1997).

To scrutinize intermittent spatio-temporal behavior, a time-dependent analysis of vortical structure is highly desirable. In the present study, the unsteady behavior of pressure fluctuations in separated and reattaching flows over a backward-facing step is examined by means of continuous wavelet transform. Endowed with the wavelet's time-localized analysis capability, the present simultaneous, multipoint measurements of the pressure fluctuations furnish a novel technique to delineate the time-dependent nature of flow field. Emphasis is placed on the modulated spatio-temporal behavior of large-scale shed vortices in low frequencies. To further facilitate an in-depth in-

*This paper was supported by a grant from the National Research Laboratory of the Ministry of Science and Technology, Korea.

vestigation of the flow mechanisms pertaining to the low-frequency flapping motion and the large-scale vortex shedding process, an experimental technique was performed by measuring a joint correlation between the velocity field and the pressure fluctuations. An adequate online pressure data processing method, termed here as the spatial box filtering, will be introduced and discussed.

EXPERIMENTAL APPARATUS

A subsonic open-circuit wind tunnel, which had been constructed in the earlier work of Chun and Sung (1996), was slightly modified for the present experiment. A detailed description about the wind tunnel can be found in LS. The step height H of the backward-facing step was 50mm and the aspect ratio $AR = 12.5$. In the present study, an Acousticel array microphone system (The Modal Shop Inc., Model TMS130A) was utilized for sensing the pressure fluctuations. This system consists of 32 electret condenser microphones, with a diameter of 10.54 mm and a height of 25.4 mm, connection cables and a 32-channel differential amplifier (Model 514A). The calibration procedure is described in detail in LS, and the calibration results indicated that the magnitude error and the phase delay were below $\pm$1dB and $\pm$3 degrees, respectively, in the frequency range from 5 Hz to 10 kHz. This 'flat' response, together with the wide dynamic range of 42-142 dB, guarantees high levels of measurement accuracy without any further compensation procedure of the Acousticel output.

In the present measurement setup shown in Fig. 1, the array which consisted of 29 Acousticel microphones was located along the centreline of the test section. The array was set up with nonuniform interval so that it spanned a streamwise extent of $9H$ from $x/H = 2.0$ to $x/H = 11.0$. The interval between each microphone was set at $0.25H$ for the reattaching region $5.0 \leq x/H \leq 10.0$, while it was $0.5H$ for other regions. As seen in Fig. 1, velocity time history was measured on an (x, y)-centreplane of the test section. The velocity measurement grid of 37×21 extended over $2.0 \leq x/H \leq 11.0$ and $0.01 \leq y/H \leq 1.6$. For the measurement of the velocity field and time-mean reattachment length x_R, the usual hot-wire technique was used together with a constant temperature anemometer (TSI-IFA300). For every velocity time history measurement, pressure time history from a total of 29 microphones were simultaneously acquired using

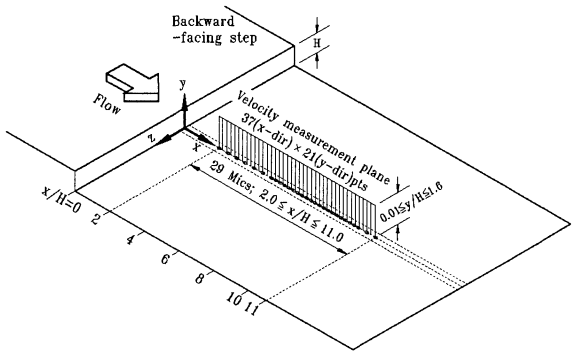

Figure 1: Schematic diagram of test section.

the 32-channel A/D converter DT2839 (Data Translation Inc.) with the effective sampling frequency of 488.28125Hz.

EXPERIMENTAL RESULTS

In the present experiment, the Reynolds number based on the step height $Re_H = 33{,}000$ is selected, which is the same as in the experiment of Chun and Sung (1996). When rescaled by using the momentum thickness, this corresponds to $Re_\theta = 1{,}300$. Among the various data representing the backward-facing step flow, the reattachment length x_R is frequently used as a representative quantity in a time-mean sense. The reattachment length is found to be $x_R = 7.4H$. Details regarding the mean and fluctuating velocity profiles and other quantities can be found in Chun and Sung (1996).

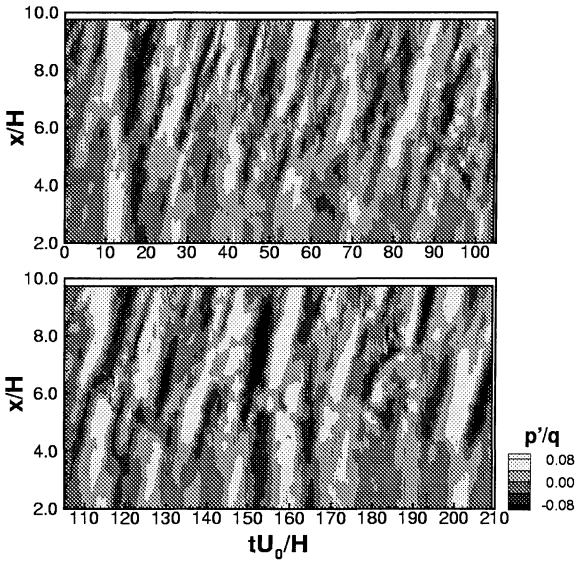

Figure 2: Space-time contour plots of pressure fluctuations.

To begin with, it would be advantageous to take a look at the global features of the space-time characteristics of wall pressure fluctuations. Figure 2 exhibit the space-time contour

plots of instantaneous wall pressure fluctuations, normalized by the freestream dynamic pressure $q = 1/2\rho U_0^2$, measured for $2.0 \leq x/H \leq 9.75$. Note that this figure consists of two 'time slides' with the upper one preceding the lower one. The downstream convective feature, denoted by an inclined contour pattern, is observed in both figures. There is no evidence of the upstream convection, which is consistent with the positive convection velocity estimation of $0.6U_0$ in LS. It is well known that the instantaneous negative peaks in wall pressure fluctuations are associated with the passage of large-scale vortices (Cherry et al. 1984, Kiya and Sasaki 1985). Also, the positive peaks are induced by the downward inrush of freestream between vortices. A closer inspection of Fig. 2 reveals that the pressure fluctuations are globally in phase and oscillate as a whole at some time instances, i.e., $tU_0/H \sim 10$ and 155. In addition, the pressure fluctuations are more intensive at this 'global oscillation' phase. Between the global oscillation phases, the convection of vortices seems to be prevailing. However, the strength and the spatial extent of each vortex are not uniform. Namely, relatively small scale behaviors are dominant at $tU_0/H \sim 40$.

To scrutinize the above modulated spatio-temporal behavior, a time-dependent analysis based on the wavelet transform is employed in this study. The wavelet transform has been extensively utilized as an analysis tool in turbulence studies. This popularity stems from the ability to elucidate both spectral and temporal information simultaneously. A comprehensive account of the mathematical and historical background of wavelet transform is given in Farge (1992). Endowed with the wavelet's time-localized analysis capability, the present simultaneous, multi-point measurements of the pressure fluctuations furnish a novel technique to delineate the time-dependent nature of flow field.

The wavelet transform $W(a,b)$ of a continuous real-valued time signal $x(t)$ is defined as the inner product between $x(t)$ and the analyzing wavelet $\psi_{a,b}(t) = (1/\sqrt{a})\,\psi((t-b)/a)$ (Farge 1992). Here, a is the timescale dilation parameter and b is the time translation parameter, respectively. Among the various wavelets proposed so far, consideration is given to a real-valued 'Mexican hat' wavelet, which is defined as, $\psi(t) = (1-t^2)\,e^{-t^2/2}$. Figure 3 shows the contour plots of wavelet transform, calculated at eight locations from the array with $X_0 = 2.0$

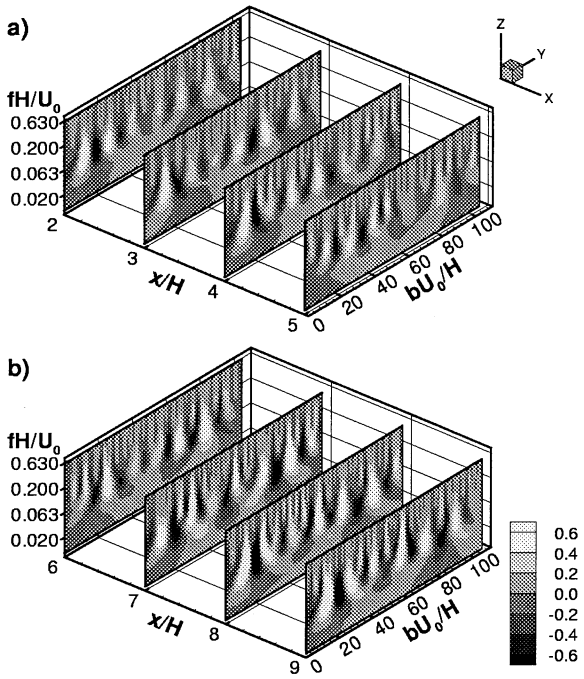

Figure 3: Contour plots of wavelet transform. a) $2.0 \leq x/H \leq 5.0$; b) $6.0 \leq x/H \leq 9.0$.

$(2.0 \leq x/H \leq 9.75)$ with the interval H. A nondimensional frequency fH/U_0 is employed on the z axis. As mentioned earlier, it is noteworthy that every plot of $W(a,b)$ has been synchronized because the pressure time histories from all points in the array are simultaneously acquired. Thus, the spatially-evolving characteristics of various frequency components can be displayed. The regular extrema along the frequency $fH/U_0 \sim 0.063$ correspond to the frequency of large-scale vortices, which was shown to be $fH/U_0 \sim 0.065$ in Fig. 3. It can be seen that this vortical component contains most energy of pressure fluctuations. This suggests that the shed vortices are largely responsible for the pressure fluctuations. The increase of rms pressure along the streamwise direction can be identified by simply comparing the maxima and minima of wavelet transform at various locations. A perusal of individual contour plots discloses that the large-scale vortical mode of pressure fluctuations undergoes energetic and quiescent phases. This tendency is evident in the forward part of the recirculation region (Fig. 3 a)).

In the reattaching region ($x/H = 8.0$ in Fig. 3 b)), the small-scale components are discernible near $bU_0/H \sim 40$. A closer inspection of both Fig. 2 and Fig. 3 b) indicates that the appearance of small scales is correlated with the initial stage of the vortex convection phase. At this stage, the separate

extrema with low and high frequencies demonstrate the breakdown of large-scale vortices. On the other hand, the contour plot exhibits simpler patterns in other stages. It seems that the frequency composition of eddies is influenced by the phase of flapping motion. Further downstream at $x/H = 9.0$, the small scale disturbances decay out and a new regular pattern is re-established. Eaton and Johnston (1981) reported the controversy between two models concerning the reattachment process; the downstream-moving small eddies in contrast to the eddies moving alternately upstream and downstream. The upstream convection has not been observed in the present wavelet transform analysis, which is consistent with the result in LS. Furthermore, the breakdown of eddies has not been observed at every large-scale vortical structure. Since the pressure fluctuations at a given point are in principle influenced by velocity fluctuations in the neighboring region of the flow, it seems to be inadequate to investigate the behavior of small scale eddies from the wavelet transform of pressure fluctuations. Nevertheless, it is obvious that the reattachment process gives rise to a multitude of events with different frequency compositions, rather than a unique predetermined one.

Since the wavelet transform is performed at each pressure time history, it may be possible to define the wavelet transform in a three-dimensional space (x, b, f). Accordingly, the isosurface of large magnitude of the wavelet transform, whose planform view is given in Fig. 4 a), represents a locus of high energy in the pressure fluctuations in space and time. The values of 0.6 and -0.6, approximately 40% of the maximum magnitude, have been chosen arbitrarily to define the isosurfaces. The alternating occurrences of the global oscillation phase and the vortex convection pahse are clearly seen in Fig. 4 a). Figure 4 b) is a cross-sectional contour plot of the wavelet transform at $fH/U_0 = 0.06458$, where the space-time variation of wavelet transform is most energetic. Note that the frequency corresponding to the most energetic scale coincides with the frequency of large-scale vortices ($fH/U_0 \sim 0.065$). At the beginning of the vortex convection phase near $bU_0/H \sim 50$, the inclined contours branch off from the vertical ones near $x/H = 4.0$. In addition, the end of the vortex convection phase is marked by a merging of the inclined contours back into the stationary vertical ones at $bU_0/H \sim 150$. These sequential phenomena can be described by the

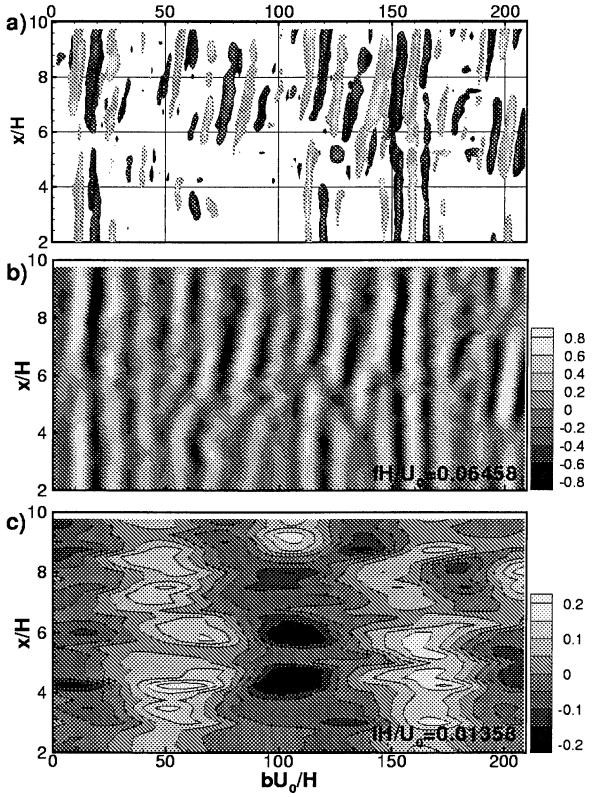

Figure 4: Planform views of wavelet transform. a) Isosurfaces; b) Contour plot at $fH/U_0 = 0.06458$; c) Contour plot at $fH/U_0 = 0.01358$.

following scenario of the large-scale vortices; firstly, a global intense oscillation appears with the contraction of separation bubble. As the bubble is enlarged, the separated shear layer receives positive momentum in the streamwise direction. After a quiescent period, a large-scale vortical structure emerges and is then accelerated to form orderly structure behind it. Secondly, these periodic vortices convect downstream. Finally, the vortices are decelerated and the next global oscillation redevelops.

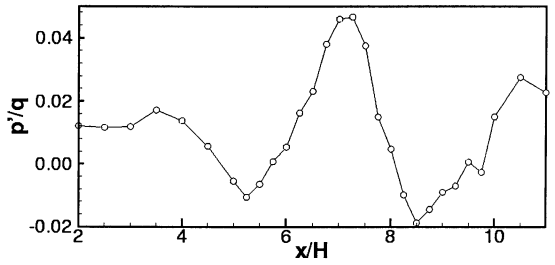

Figure 5: Streamwise distribution of the conditionally averaged pressure fluctuations.

The advantage of mulit-point pressure information over single point measurement as a conditioning signal is the immunity to irrelevant small scale mode contributions. In this respect, a relevant pressure component associated with the coherent structures in the flow

field could be found on the basis of the measured spatio-temporal distribution of pressure fluctuations. Toward this object, the appropriate length scale of the pressure field are to be found. This is implied in Fig. 5, where the streamwise distribution of conditionally averaged pressure fluctuations, normalized by the inflow dynamic pressure $(1/2\rho U_0^2)$, is presented. Time is synchronized with the the time when the transverse velocity fluctuations v' at $(x, y) = (7.5H, 1.0H)$ exceeds $-2.5v_{rms}$. It is seen that there exist a negative correlation between the pressure and v', and the pressure peak associated with the excursion of transverse velocity is of the order of $1.5p_{rms}$. The spatial distribution, the main peak surrounded by the negative upstream and downstream valleys, is attributable to the large-scale vortical structure. Kiya and Sasaki (1985) demontrated that the positive excursion of pressure fluctuation was shown to coincide with the inrush of the outer irrotational fluid with high total pressure towards the wall. The negative excursion of the transverse velocity imposed as the conditioning signal was indeed set toward to this inrush, the similarity between the two waveforms suggests that the conditional average of Fig. 5 results from the large-scale vortical structure. In this figure, and the spacing between the two valleys, which can be regarded as the spacing between large-scale vortices, is approximately $4H$. This spacing corresponds to $0.54x_R$, which is close to $0.6x_R$ reported by Kiya and Sasaki (1985).

From the above observation, it can be stated that the spatial mode of pressure fluctuations associated with the large-scale vortical structure attains a streamwise scale of $4H$. Of course, this is not to oversimplify the reattaching flow processes as a series of two-dimenisonal spanwise rollers. It is certain that the reattaching flow exhibits such inherent three-dimensionality as hairpin vortices and stremwise vortices in the shear layer, which was demonstrated by many researchers (Kiya and Sasaki 1985, Shih and Ho 1994, Le et al. 1997). However, it is no doubt that the most dominant source of pressure fluctuations is the spanwise large-scale vortical structure in the shear layer.

In order to extract a specific spatial component of the pressure field, a spatial box filtering (denoted as SBF hereinafter) is introduced in this study, whose schematic is given in Fig. 6. As depicted in Fig. 6, 16 equally-spaced microphones, with uniform spacing $\Delta x/H = 0.5$,

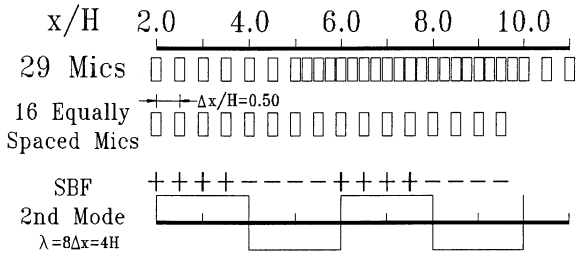

Figure 6: Schematic diagram of Spatial Box Filtering

out of whole 29-element array are utilized. The specific mode $\tilde{p}^{(i)}$ which corresponds to the spatial wavelength λ_i is obtained by a weighted sum of p_k, pressure at kth sensor, with a spatial filter function $w_k^{(i)}$ as follows:

$$\tilde{p}^{(i)} = \sum_{k=0}^{N-1} p_k w_k^{(i)}, \quad w_k^{(i)} = (-1)^{[k/2^{4-i}]}. \quad (1)$$

Here N is the number of sensor and $[\cdot]$ represents truncation to nearest smaller integer. Thus, the waveform of $w_k^{(i)}$ is a square wave whose wavelength λ_i is given as $2^{5-i}\Delta x = 2^{4-i}H$. The spatial box filtering (SBF) based on $w_k^{(i)}$ defined in the above equation is a wavenumber filtering tuned for a specific wavelength λ_i. As depicted in Fig. 6, the wavelength of $w_k^{(2)}$ is $4H$, the length scale of large-scale vortical structure. Therefore, the SBF 2nd mode of pressure $\tilde{p}^{(2)}$ represents the wavenumber components which is associated with the large-scale vortical structure.

The conditionally averaged velocity time histories $\langle u \rangle / U_0$ and $\langle v \rangle / U_0$ measured at $(x, y) = (7.5H, 1.0H)$ based on the SBF 2nd mode of pressure $\tilde{p}^{(2)}$ is shown in Fig. 7 a) and b), respectively. The conditional average based on the pressure fluctuations at $x/H = 7.5$ (denoted as p_R hereinafter) is also plotted as dashed line for comparison. The time is synchronized with the instants when the two conditioning signal, $\tilde{p}^{(2)}$ and p_R attains a peak over 2.5 times rms level of each signal. It is notable that the conditional averages based on $\tilde{p}^{(2)}$ show larger velocity excursions compared to those associated with local pressure peak. This implies that the randomness in the conditional average, which stems from the 'improper' conditioning peak in local pressure signal, i.e., pressure peaks uncorrelated with the coherent flow structures, has been reduced by means of utilizing an organized conditioning signal of SBF 2nd mode. The conditional averages in Fig. 7 show no appreciable information far from the zero time, say, $|tU_0/H| > 15$ due

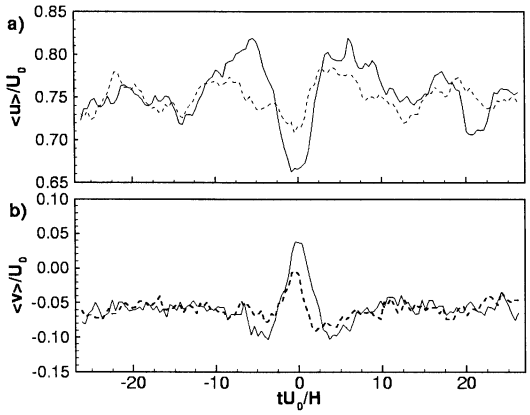

Figure 7: Comparison of the conditionally averaged velocity time history. ——, Conditional average based on $\tilde{p}^{(2)}$; - - -, based on the positive peak of p' at $x/H = 7.5$. a) $\langle u \rangle / U_0$; b) $\langle v \rangle / U_0$.

to the increasing uncertainties with respect to the increase in the time difference. However, the conditionally averaged velocity excursions based on both signal become nearly coincident, although not exactly. From this, the conditioning signal of $\tilde{p}^{(2)}$ can be regarded to be largely in phase with the coherent component near the time-mean reattachment point $x_R/H = 7.4$. In summary, it can be stated that $\tilde{p}^{(2)}$ is more closely associated with the pressure-generating coherent flow structure than the pressure a single location. Furthermore, this pressure mode is readily applicable to the a non-intrusive online investigation of the large-scale vortical structures.

CONCLUDING REMARKS

Unsteady characteristics of wall pressure fluctuations in the separated and reattaching flows over a backward-facing step and their relationship between relevant flow modes have been described by means of a variety of signal processing methods. In the present study, the wavelet analysis of pressure time histories from an array of microphones elucidated various evolutionary features of flow field. It was found that the periodic maxima and minima of the wavelet transform are mainly concentrated at the frequency of large-scale vortical structure. The shed vortices play a major role in generating the pressure fluctuations. There exist two modes of shed vortices; one is the global oscillation and the other is the vortex convection. These are synchronized with the flapping frequency component of pressure fluctuations p_F and a possible scenario of the vortical motion is then proposed. From the space-time information of the pressure fluctuations, an effective means to extract relevant spatial mode due to the large-scale vortical structure has been introduced and discussed. This is termed as spatial box filtering (SBF) and the emphasis is given to the SBF 2nd mode of pressure $\tilde{p}^{(2)}$ with the wavelength corresponding to the length scale of the large-scale vortical structure. The conditional average of velocity fluctuations based on $\tilde{p}^{(2)}$ reveals that this mode is better correlated with the pressure-generating eddies than the pressure at a single location.

REFERENCES

Cherry, N. J., Hillier, R. and Latour, M. E. M. P., 1984, "Unsteady measurements in a separated and reattaching flow", *J. Fluid Mech.*, Vol.144, pp.13-46

Chun, K. B. and Sung, H. J., 1996, "Control of turbulent separated flow over a backward-facing step", *Exp. Fluids*, Vol.21, pp.417-426.

Eaton, J. K. and Johnston, J. P., 1981, "A review of research on subsonic turbulent flow reattachment", *AIAA J.*, Vol.19, pp.1093-1100.

Eaton, J. K. and Johnston, J. P., 1982, "Low frequency unsteadiness of a reattaching turbulent shear layer", *Turbulent Shear Flows*, Vol.3, pp.162-170.

Farge, M., 1992, "Wavelet transforms and their application to turbulence", *Ann. Rev. Fluid Mech.*, Vol.24, pp.395-437.

Kiya, M. and Sasaki, K., 1985, "Structure of large-scale vortices and unsteady reverse flow in the reattaching zone of a turbulent separation bubble", *J. Fluid Mech.*, Vol.154, pp.463-491.

Le, H., Moin, P. and Kim, J., 1997, "Direct numerical simulation of turbulent flow over a backward-facing step", *J. Fluid Mech.*, Vol.330, pp.349-374.

Lee, I. and Sung, H. J., 2001, "Characteristics of wall pressure fluctuations in separated flows over a backward-facing step Part. I Time-mean statistics and cross-spectral analyses", *Exp. Fluids*, Vol.30, pp.262-272.

Shih, C. and Ho, C. M., 1994, "Three-dimensional recirculation flow in a backward facing step", *J. Fluids Eng.*, Vol.116, pp.228-232.

A SPATIAL STRUCTURE OF A FLOW OF AXISYMMETRIC SUDDEN EXPANSION

Noriyuki Furuichi and Yasushi Takeda
Paul Scherrer Insitut
CH5232 Villigen PSI, Switzerland
Noriyuki.Furuichi@psi.ch, Yasushi.Takeda@psi.ch

Masaya Kumada
Gifu Univ.
1-1 Yanagido, Gifu, 501-1193, Japan
kumada@cc.gifu-u.ac.jp

ABSTRACT

A flow transition for an axiymetric sudden expansion was experimentally investigated. Spatio-temporal flow field measured using ultrasonic velocity profiler and analyzed by a two-dimensional Fourier transform and a proper orthogonal decomposition. The variation of the zero-cross point of the axial velocity distribution, the energy of velocity fluctuation directed to upstream and the eigenmode spectrum have the same transitional scheme with respect to Reynolds number. The transitional scheme can be classified as laminar flow for Re_d <1000, and transitional regime for Re_d =1000-4000 and turbulent regime for Re_d >4000. We found that the two large change occurs in the transitional regime at around Re_d =1500 and 2000. The jump that occurs at Re_d =2000 is caused by the change of the flow condition in the upstream pipe. The jump at Re_d =1500 shows a change of the spatial structure of the flow.

INTRODUCTION

A flow structure in a pipe with a symmetric sudden expansion has been studied in the past as it is frequently encountered in engineering practice. Concerning the fundamental fluid mechanical characteristics in this configuration, it has a complexity of the internal flow separation and reattachment.

It is well known that a time averaged reattachment length varies as a function of a Reynolds number. Some researchers investigated its behavior because it is one of the most important features of this flow field (Back and Roschke 1972, Eaton and Johnston 1981, Armly et al. 1983, Adams and Johnston 1988). The averaged reattachment length increases steadily for laminar regime ($Re \leq 10^3$) and decreases in the transitional regime. At higher Reynolds number ($Re \geq 10^4$; turbulent regime), it increases slightly with increasing Reynolds number. The flow mechanism of the laminar and turbulent regime have already been understood quantitatively well. For a laminar region, the averaged reattachment length obtained by recent numerical experiments is in a good agreement with those by experiments. (Lewis and Pletcher 1986, Abe et al 1994). On the other hand, for a transitional regime, the averaged reattachment length have large difference among many experiments. A behavior of variation of the reattachment length as a function of Reynolds number of this regime shows complex change as reported by Armly et al.(1983), but it has not been investigated enough by taking into account a change of the spatial structure.

It is also well known that there exists a low-frequency astationary motion, usually called "flapping" of the separated shear layer. This phenomenon appears to be strongly related to a concentration of the separated shear vortex and the fluctuation of the instantaneous reattachment point (Driver et al, 1985). In many previous reports, the experimental results such as velocity profile or turbulent intensity were obtained as a function of wall normal direction (like $v_z(r)$). Moreover, no temporal characteristics were considered. However, for investigating detail structure of the flapping in relationship with the reattachment, it is necessary to obtain a streamwise velocity distribution as a function of streamwise direction and time (like $v_z(z,t)$).

In this investigation, we used a ultrasonic velocity profiler (UVP) to obtain spatio-temporal velocity fields on the streamwise direction ($v_z(z,t)$) in the axisymmetric sudden expansion and analyzed them by a two-dimensional Fourier transform and the proper orthogonal decomposition (POD method). Since various modes can be observed in this flow field such as flapping, growth and shedding of the separated shear vortex and recirculation flow, it is important to analyze the flow field by making use of field decomposition by these methods. We investigated a behavior of transition sequence of the flow field from laminar to turbulent regime by evaluating the contribution of each modes to the total turbulent energy.

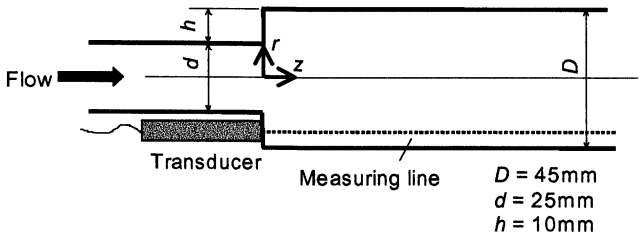

Figure 1. Experimental setup

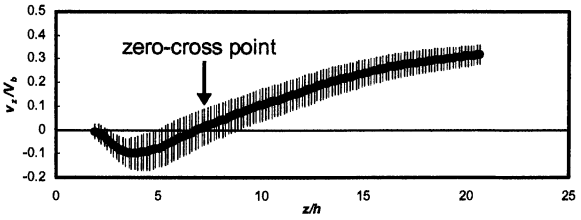

Figure 2. Example of an averaged velocity profiles at Re_d=3591

EXPERIMENTAL SETUP AND METHOD

Experimental apparatus and coordinate system is illustrated in Figure 1. The pipe diameter of the upstream of the step is d=25mm and is D=45mm at downstream. The step height is then h=10mm and the expansion ratio is ER=1.8. The sudden expansion is located at $84d$ downstream from the flow conditioner. The control parameter is $Re_d = dV_b/\nu = 5.0\times10^2 \sim 1.5\times10^4$, where d is the upstream pipe diameter and V_b a bulk velocity estimated from flow rate. The velocity profile in the upstream channel before entering the sudden expansion is fully developed and the critical Reynolds number is $Re_c \approx 2.0\times10^3$ in this experiment.

The measurements were carried out with a ultrasound velocity profiler (Takeda, 1990) which can obtain time series of instantaneous velocity profiles. One instantaneous velocity profile consists of 128 data points. The ultrasonic transducer was set at r/h=1.75 as shown in the Figure 1 and measured a streamwise velocity component (v_z) as a function of z and time ($v_z(z,t)$). The distance between two measurement points is 1.48mm and measured range is z/h=2~20. A typical time to obtain one velocity profile is about 70msec and total measuring time is 573 second (8192 profiles).

RESULT AND DISCUSSION

Velocity field – Average profile

Before discussing spatio-temporal nature of the flow, we start to use time averaged velocity profiles. A typical example is given in Figure 2 together with turbulent intensity at Re_d=3591. It shows a smooth velocity profile. In most of previous works, the averaged velocity profile was measured as a function of wall-normal axis as $V_z(r)$, and then the measurement points for streamwise direction was very coarse. A typical velocity profile has two regions of positive and negative velocity values. It is easily justified that the region of negative velocity corresponds to a so-called recirculation bubble, and its spatial structure can be evaluated quantitatively from a zero-cross point of those averaged profiles.

A behavior of a reattachment phenomenon is normally characterized by a reattachment length. Many of the previous investigations performed measurements of a variation of the reattachment length as a function of a Reynolds number. However an increment of the measured Reynolds number is

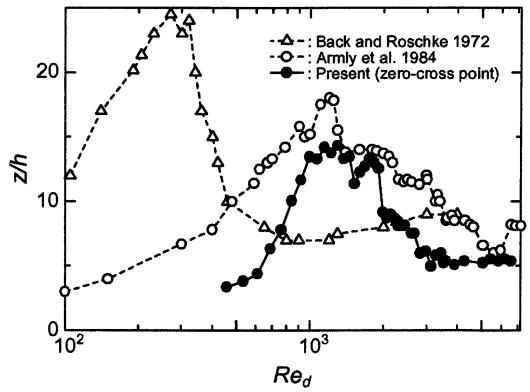

Figure 3. Variations of the zero-cross point and the reattachment point

large. The most detailed work might be of Armly et al(1984) on two-dimensional backward-facing step. They measured a reattachment length for a wide range of Reynolds number using laser Doppler anemometry. They summarized the tendency of the variation of the reattachment length as following (cf. Figure 3); The laminar regime of the flow is characterized by a reattachment length that increases with Reynolds number (based on the hydraulic diameter). The regime of transitional flow (Re=1200-6000) is characterized by a sharp decrease in the reattachment length, by irregular decrease to a minimum value at a Reynolds number of approximately 5500, then an increase to a constant level. The turbulent regime is then characterized by a constant reattachment length.

We measured streamwise velocity profiles with much finer distance of data points of z so that we can obtained the zero-cross point of the velocity profile, as shown in Figure 2, with much higher precision. Although this value is not the same physical value as a reattachment length because its radial position pf the ultrasonic beam is slightly away from the wall, it can be compared reasonably with other investigations. Figure 3 shows a variation of the zero-cross point. The general tendency of the variation of the zero-cross point is in good agreement with a change of reattachment length (Armly et al.). For a region from Red=1000-2000, there are two maxima. The first maximum is seen at $Re_d \approx 1500$, and the second at $Re_d \approx 2000$. The second might be due to the change of upstream flow condition to turbulence since it happens at a critical Reynolds number of

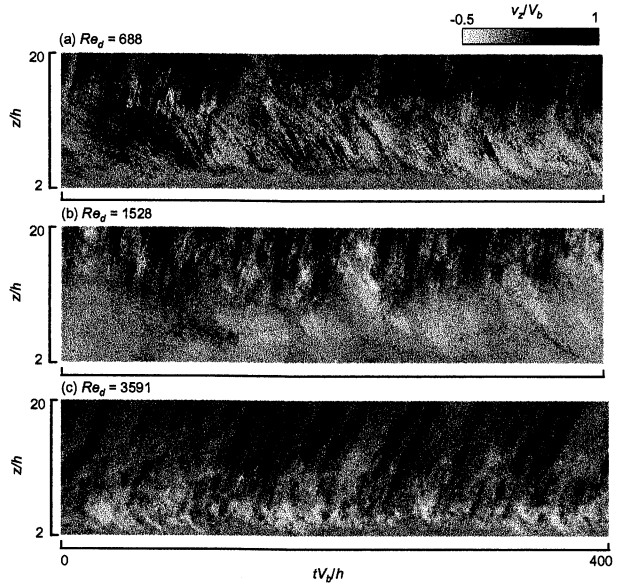

Figure 4. Examples of measured velocity fields

about 2000. However, the mechanism of the first increase can not be explained from the averaged velocity profile. For Re_d =2000-4000, it decreases irregularly and is considerably stable for Re_d>4000. For a later discussion, we call the regime of Re_d <1000 a laminar regime, Re_d =1000-3000 a transitional regime, Re_d>3000 a turbulence regime.

Spatio-temporal velocity profile

As examples of the spatio-temporal velocity field, a two-dimensional gradation map of $v_z(z,t)$ velocity a component are shown in Figure 4. The horizontal axis is a normalized time and vertical axis is a position normalized by a step height. The gradation changes from white to black as increasing velocity. The stripes of positive gradient means a flow (vortices) directed to downstream and one of negative gradient means a upstream flow. With an overall view, vortices are traveling to downstream for z/h=10~20. A large scale structure around the separated shear layer is observed for z/h=5~10, where the flow direction changes as time, namely a strong spatial fluctuation of instantaneous zero crossing point. These figures show clearly a change of such a flow structure in each regime. The recirculation region observed in the Figure (b) is larger than that in (a) as increasing Reynolds number. It becomes smaller and the gradient of the stripes is smaller in figure (c).

Examples of the local power spectra of the streamwise velocity fluctuation are shown in Figure 5. The Reynolds number and the spatial location are given in the figure. These locations correspond to the averaged zero-cross point. Although it is said that the low-frequency fluctuation is dominant in these locations (around a reattachment region), we found that no typical peak can be seen for these Reynolds number.

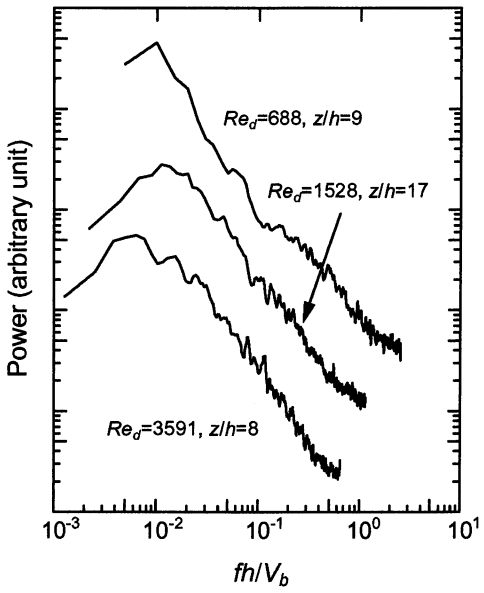

Figure 5. Example of the power spectra of the velocity fluctuation

Two-dimensional Fourier transform

As shown in Figure 4, a structure of which motion directs to downstream and upstream exists in the same region of the flow field. The vortex shed from the separated shear layer travels to downstream, while a part of recirculation bubble flows to upstream, and as a result its boundary and the reattachiment point fluctuates in spatio-temporal manner. For investigating quantitatively the nature of this complicated flow field, a time-domain Fourier analysis (power spectra) is not sufficient as shown in Figure 5. We then used a two-dimensional Fourier analysis. As the energy of velocity fluctuation traveling to downstream and upstream can be obtained separately by this method, it would be suited for analysis of this flow filed. We computed the spectrum of the velocity fluctuation by following formula.

$$S(k,f) = \int_{-\infty}^{\infty}\int_{-\infty}^{\infty} v_z(z,t)e^{-ikz}e^{-ift}dzdt \qquad (1)$$

where f is frequency and k is wave number. With respect to the space and time resolution, we can obtain a two-dimensional Fourier spectrum on the plane of f =[0, 7.042](Hz) and k=[0, 0.337](mm^{-1}) with resolution of [0.013Hz, 0.003mm^{-1}].

Examples of the spectra of the two-dimensional Fourier transform are shown in Figure 6. The abscissa is frequency and the coordinate is wave number. Negative value of the wave number is also plotted so that flow direction can be accounted. Namely, the first domain depicts the spectrum of the flow that directs to downstream and the forth is to upstream. Reflecting the velocity fluctuation caused by the vortex that is traveling to downstream with

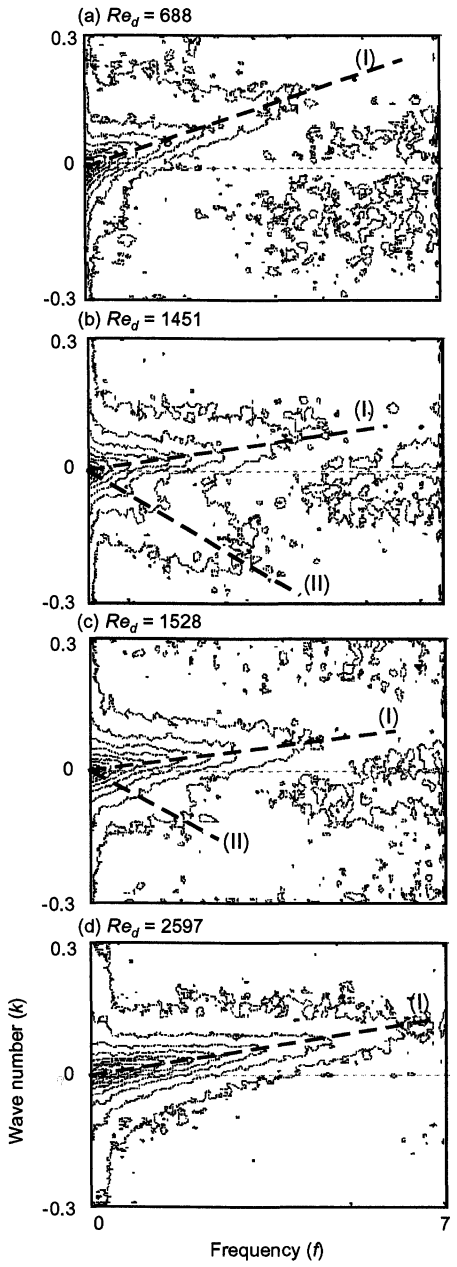

Figure 6. Contour maps of the two-dimensional Fourier transform

constant velocity, the energy concentration is shown clearly on each figures as a line (shown as (I)). In (b), by comparing figure (a), a line of negative gradient appears (dotted line; II), which corresponds to the flow directed to upstream. This feature can also be seen in figure (c), which is much smaller than in (b). In the turbulent regime (figure (d)), the energy is more concentrated on the vortex structure and no upstream flow is observed. It is, concludingly, clear that it is a characteristic phenomenon appearing only in the transition regime.

A gradient of the lines on the two-dimensional Fourier spectrum corresponds to the convection velocity of the vortex traveling to downstream. The variation of the convection velocity thus estimated from those spectra is shown in Figure 7. In the laminar and the transitional regime, the obtained

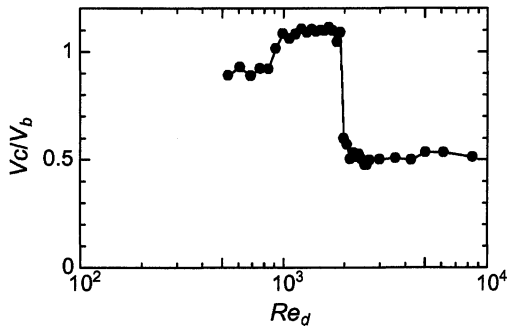

Figure 7. Convection velocity directed to downstream (normalized by the bulk velocity)

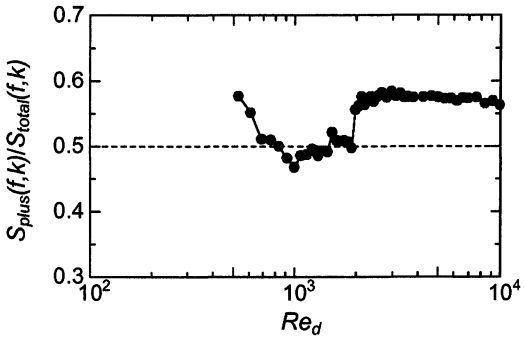

Figure 8. Relative power of velocity fluctuation directed to downstream

convection velocity is more or less equal to the main flow. This indicates that the vortex shedding is caused by the shear layer. On the other hand, it shows a sudden change at $Re_d \approx 2000$ down to the half of the bulk velocity, indicating a generation of larger vortex outside the shear layer. This result for the turbulent regime is in good agreement with the previous reports. (Hijikata et al. 1990, Furuichi et al. 1999).

To observe a contribution of the energy for each direction, a variation of the energy of flow directed to downstream relative to the total energy is shown in Figure 8. The total energy is defined as the summation of $S(f,k)$ over the whole domain and the energy directed to downstream is a summation of the power in the first domain. The transition behaviour is seen also in this figure; similar to the variation of the zero-cross point. The fraction of the energy directed to downstream decreases at $Re_d \approx 1000$, and is almost constant for Re_d =1000-2000 except for a small jump at Re_d =1500. There is observed a large jump at Re_d =2000. It corresponds to the sharp decrease of the zero-cross point shown in Figure 3.

Figure 9 shows reconstructed spatio-temporal velocity fields. These velocity fields are reconstructed only for the flow directed to downstream of which the convection velocity is (a)$1.1V_b$ and (b)$0.5V_b$ (all other component is filtered out). It shows clearly a vortex motion that is traveling to downstream and the difference of the convection velocity between two flow regimes. In figure (a), this motion has a fairly high periodicity and estimated Strouhal number $St = fh/V_b$ =0.2, where f was estimated from power

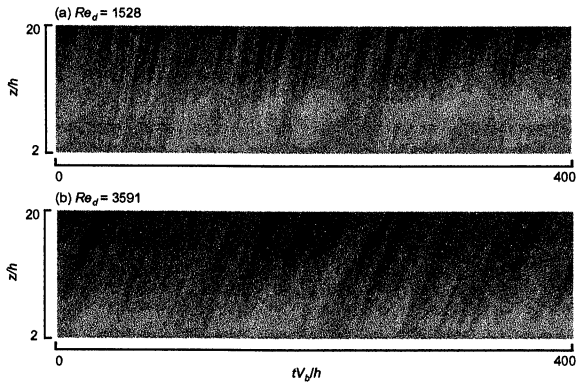

Figure 9. Reconstructed velocity field

spectrum of this velocity profile. On the other hand, periodical structure is weak in figure (b) and the low frequency fluctuation is dominant (St=0.02). This is consistent with previous investigations by Eaton & Johnston (1981).

Orthogonal decomposition

As discussed earlier, this flow field is less periodic in spatial and/or temporal domain so that Fourier analysis is less effective. To identify the coherent structure of this flow field, the POD (proper orthogonal decomposition) method would be better suited since the dominant structure involves higher engenmodes. At the same time, the eigenspectrum might be used to investigate the change of the structure. The method is based on the decomposition of the fluctuating velocity field into a sum of mutually orthogonal engenfunctions of the two-point correlation tensor. This method has been applied by many researchers to various flow fields. (Delville et al. 1990, Takeda 1999)

We decomposed the streamwise velocity field (z-t field) by the following formula;

$$v(z,t) = \sum_n a^{(n)}(t)\phi^{(n)}(z) \qquad (2)$$

where $\phi^{(n)}(z)$ are eigenfunctions, $a^{(n)}(t)$ are un-correlated random coefficients of eigenvalues ($\lambda^{(n)}$). The contribution of each structure to the turbulent kinetic energy and total energy (E) in the measurement region (D:z/h=2-20) can be determined as

$$\left\langle v^2(z)\right\rangle = \sum_n \lambda^{(n)}\phi^{(n)2}(z) \qquad (3)$$

$$E = \int_D v^2(z)dz = \sum_n \lambda^{(n)} \qquad (4)$$

The variation of eigenvalues for the first 10 strongest modes is shown in Figure 10 with respect to Reynolds number. The 0th mode decreases in laminar regime and other modes increase as increasing Reynolds number. In the transitional regime, the eigenvalue of 0th and 1st modes jump up at Re_d =2000. This corresponds to a large change in

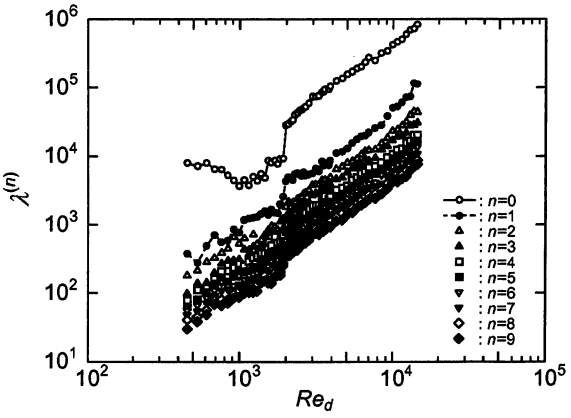

Figure 10. Variation of 10 eigenvalues

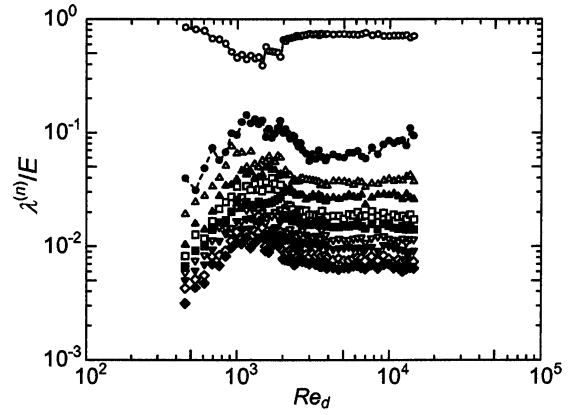

Figure 11. Variations of normalized eigenvalue

the reattachment length at this Re number; see Figure 3. Furthermore, there is seen a smaller jump at Re_d=1500. This feature of two step increase of eigenvalues appears to correspond to the existence of two maxima in the variation of the reattachment length. For the turbulent regime (Re_d>3000), the energy increases steadily and no large change is seen.

In order to see a contribution of the energy of each mode, the variation of the eigenvalues for the first 10 eigenmodes normalized by the total energy of the eigenvalues ($\lambda^{(n)}/E$) is plotted in Figure 11. For laminar regime, the fraction of the energy of the 0th mode decreases while those of other modes increase with Reynolds number. In the transition regime, it is clearly seen that the energy of 0th mode decreases while those of higher modes increases, showing a local minimum for 0th mode and local maxima for other modes. This indicates that a considerably large fraction of total energy is occupied by higher modes. It may imply an energy transfer from the base mode to the higher mode in this regime.

Aubry et al.(1994) proposed another way to use the information in the eigenvalue spectrum to identify changes in flow behavior as following formula

$$H = -\frac{1}{\ln N}\sum_n p^{(n)} \ln p^{(n)} \qquad (5)$$

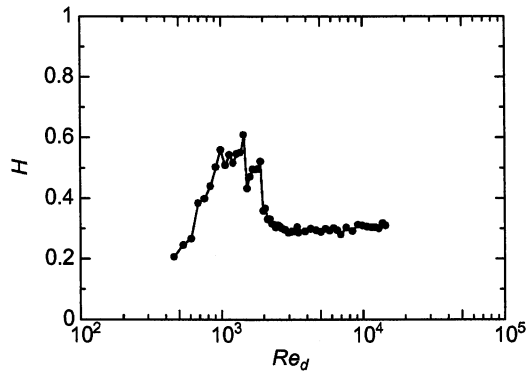

Figure 12. A variation of the global entropy

where H is a global entropy and $p^{(n)} = \lambda^{(n)}/E$. N is the number of data points. H=0 corresponds to perfectly ordered state and H=1 corresponds to the completely disordered state. A variation of the global entropy of our data is shown in Figure 12 with respect to Reynolds number. It shows also a typical transitional scheme as discussed above. Namely H is large for the transition regime with two maxima. For the laminar regime, the global entropy increases steadily, and for Re_d >3000, it is quite constant.

CONCLUSION

Spatio-temporal velocity field of the axiymetric sudden expansion was experimentally investigated using ultrasonic velocity profiler and analyzed by two-dimensional Fourier transform and proper orthogonal decomposition to investigate transitional scheme of the spatial structure.

The zero-cross point for Re_d <1000 increases steadily as increasing Reynolds number. It decreases suddenly at two Reynolds numbers, at Re_d =1500 and 2000. For Re_d =2000-3000 it decreases slightly and Re_d >3000 it stays constant.

A variation of the energy of the velocity fluctuation directed upstream and downstream was studied using two-dimensional Fourier transform. It has also the same transitional scheme as that of the zero-cross point. POD was also performed. It was found that there are two local maxima at Re_d=1500 and 2000 in the variation of fractional energy with Reynolds number. This is also oberserved in the variation of global entropy. The first jump at Re_d =1500 indicates clearly a change of the spatio-temporal structure in the transitional scheme. The second jump at Re_d =2000 might be caused by the change of the flow condition upstream pipe.

References

Abe, K., Kondoh, T., Nagano, Y., A new turbulence model for predicting fluid flow and heat transfer in separating and reattaching flows - I. Flow flied calculations, *Int. J. Heat Mass Transfer*, 37, 139-151, 1994

Adams, E.W., Johnston, J.P., Effects of the separating shear layer on the reattachment flow structure, Part2:Reattachment length and wall shear stress, *Exp. In Fluids*, 6, 493-499, 1988

Armly, B.F., Durst, F., Pereira, J.C.F., Schönung, B., Experimental and theoretical investigation of backward-facing step flow, *J. Fluid Mech.*, 127, 473-496, 1983

Aubry, N., Chauve, M.P., Guyonnet, R., Transition to turbulence on rotating flat disk, *Phys. Fluids*, 6, 2804-2814, 1994

Back, L.H., Roschke, E.J., Shear-layer flow regimes and wave instabilities and reattachment lengths downstream of ana abrupt circular channel expansion, *J. of Applied Mech.*, 39, 677-681, 1972

Delville, J., Bellin, S., Bonnet, J.P., Use of the proper orthogonal decomposition in a plane turbulent mixing layer, Turbulence and Coherent Structures, 75-90, 1990

Driver, D.M., Seegmiller, H.L., Marvin, J.G., Time-dependent behavior of a reattachment shear layer, *AIAA J.*, 25, 7, 914-919, 1987

Eaton, J.K., Johnston, J.P., A review of research on subsonic turbulent flow reattachment, *AIAA J.*, 19, 1093-1100, 1981

Furuichi, N., Hachiga, T., Hishida, K., Kumada, M., A vortex structure of a two-dimensional backward-facing step by using advanced multi-point LDV, Proc. of 1 st symposium of Turbulence and Shear Flow Phenomena, 1045-1050, 1999

Hijikata K., Mimatsu, J., Inoue, J., A study of wall pressure structure in a backward step flow by a holographic / velocity-pressure cross-correlation visualization, ASME-FED, 128, Experimental and Numerical Flow Visualization, 61-68, 1991

Lewis, J.P., and Pletcher, R.H., Limitations of the boundary-layer equations for predicting laminar symmetric sudden expantion, *J. of Fluid Eng.*, 108, 208-213, 1986

Takeda, Y., Development of ultrasound velociry profile monitor, Nuc. Eng. Des., 126, 177-284, 1990

Takeda, Y., Quasi-periodic state and transition to turbulence in a rotating Couette system, *J. Fluid Mech.*, 389, 81-99, 1999

Author index volume III

Agrawal, A., 53
Al-Shannag, M., 351
Alfredsson, P.H., 215
Amitay, M., 387
Angele, K., 203
Antonia, R.A., 239, 245
Antonov, T., 269
Bailey, S.C.C., 101
Bertoglio, J.P., 273
Bézard, H., 173
Bisceglia, S., 239
Boiko, A.V., 233
Borg, A., 357
Breuer, M., 393
Casciola, C.M., 251
Chaouat, B., 179
Chassaing, P., 59
Cheng, S.-I., 285
Cho, J., 47
Choi, J.-I., 11
Choi, Y.D., 345
Choi, H., 35
Chun, K.H., 345
Cushner, J., 351
Dasi, L.P, 209
Dreizler, A., 363
Driver, D.M., 107
Fornaciari, N., 215
Frick, P., 269
Fuchs, L., 357
Fureby, C., 309
Furuichi, N., 417
Gatski, T.B., 1
Giralt, F., 351
Girimaji, S.S., 185
Glezer, A., 387
Gorokhoski, M., 257
Goto, S., 263
Grinstein, F.F., 309, 333
Gualtieri, P., 251
Gutmark, E.J., 333
Herrero, J., 351
Holloway, A.G.L., 95, 191
Hosoda, T., 155
Hsiao, G., 333
Humphrey, J., 351
Ichijo, M., 221
Ishino, Y., 327
Iwamoto, K., 17
Iwase, S., 131
Jacobitz, F.G., 83
Janicka, J., 315, 363
Jiang, X., 297
Johnston, J.P., 119
Joly, L., 59
Joseph, D.D., 35
Jovicic, N., 393
Kalaev, V.V., 381
Kasagi, N., 17
Kassinos, S.C., 149
Kawamura, H., 375
Kempf, A., 315
Khan, Z.U., 119
Kida, S., 263
Kim, D.C., 345
Kimura, I., 155
Kobayashi, T., 291
Komori, S., 321
Kopp, G.A., 101
Kosovic, B., 161
Kumada, M., 417
Kunugi, T., 71
Kurbatski, A., 89
Lageneste, de, L.D., 339
Lamballais, E., 125
Langer, C.A., 149
Larsen, P.S., 143
Lee, I., 411
Leschziner, M.A., 399
Li, H., 137
Lindborg, E., 47
Long, C.H., 65
Lozhkin, S., 269
Luo, K.H., 297
Marcouyre, M., 113
Marini, B., 369
Marsden, J.E., 161
Martinuzzi, R.J., 101
Mateer, G.G., 107
McIlwain, S., 113
Menon, S., 303, 309
Meyer, K.E., 143
Michioka, T., 321
Min, T., 35
Miyauchi, T., 131
Muhammad-Klingmann, B., 203
Mohseni, K., 161
Mongia, H.C., 333

Mosier, B.P., 119
Nagano, D., 375
Neumann, J., 29
Oberlack, M., 279
Ochiwa, N., 327
Ohta, K., 227
Okamoto, M., 167
Onda, S., 155
Onishi, R., 321
Orellano, A., 29
Orlandi, P., 245
Özcan, O., 143
Park, N., 291
Peters, N., 279
Pitsch, H., 339
Piva, R., 251
Pollard, A., 113
Poroseva, S.V., 149
Prasad, A.K., 53
Rahman, S., 209
Reinaud, J., 59
Repp, S., 363
Reynolds, W.C., 149
Roach, D.C., 95, 191
Romano, G.P., 239
Rossi, L., 23
Sabelnikov, V., 257
Sadiki, A., 315, 363
Sankaran, V., 303
Satake, S., 71
Schiestel, R., 179
Schneider, C., 315, 363
Serizawa, A., 71
Shao, L., 273
Shima, N., 167
Shizawa, T., 227
Shkoller, S., 161
Silvestrini, J.H., 125
Simpson, R.L., 65
Smirnov, E.M., 381
Smith, C.R., 369
Sokoloff, D., 269
Squires, K.D., 405
Sudarsan, R., 351
Sung, H.J., 11, 411
Suzuki, Y., 17
Takeda, Y., 417
Talamelli, A., 215
Tanahashi, M., 131
Tanaka, S., 375
Taniguchi, N., 291
Temmerman, L., 399
Thibault, J.-P., 23
Touil, H., 273
Tseng, C.-H., 41
Ueno, I., 375
Wasistho, B., 405
Webster, D.R., 209
Weller, H., 309
Wengle, H., 29
Wenzel, H., 279
Westergaard, C.H., 143
Westin, K.J.A., 215
Widlund, O., 197
Wunsch, S., 77
Yamaguchi, S., 327
Yamamoto, Y., 71
Yoo, J.Y., 35
Young, Y., 77
Young, T.R., 333
Yu, M.-H., 41
Zhmakin, A.I., 381
Zhou, Y., 137
Zhou, T., 239